


Geant4 Simulations to Characterize Low-Energy Charged Particle Scattering on Flat Material Surfaces

The University of British Columbia
Dept. of Physics & Astronomy
IPP Summer Student Fellowship Program (CERN Summer Student Programme)
June 2023 - August 2023

By

Dean Ciarniello
The University of British Columbia, Dept. of Physics & Astronomy
Combined Honours in Physics and Mathematics

Performed at:
CERN, Geneva, Switzerland

Supervisor(s): Dr. Massimo Giovannozzi
CERN, BE-ABP (Accelerator and Beam Physics)

Geant4 Simulation and Characterisation of Low-Energy Charged Particle Scattering on Flat Material Surfaces

Dean Ciarniello
The University of British Columbia
Dept. of Physics & Astronomy

Supervisor(s): Dr. Massimo Giovannozzi

Abstract

As a recipient of an IPP Summer Student Fellowship for the summer of 2023, the second half of the term was spent working with the Accelerator and Beam Physics Group of the Beams department at CERN in Geneva, Switzerland, as part of the CERN Summer Student Programme. My project consisted of Geant4 simulation and data analysis of low-energy charged particle scattering off of various flat material surfaces, with the goal of characterising such scattering and applying our findings to tapered capillaries for bean density enhancement and potential beam cooling. In the early 2010s, studies at the RIKEN-RAL muon facility and the TRIUMF M9B muon beamline demonstrated the use of tapered capillaries to improve muon beam density. We developed a Geant4-based code to simulate the internal reflection experienced by such particles. Analysis of these simulations revealed unique and unexpected reflection behaviour of muons, electrons, and protons in the 10 MeV/c to 500 MeV/c momentum range, when scattered off various different elemental, composite and coated materials. In addition, we develop a second simulation framework to test tapered capillaries of linear, polynomial, and hyperbolic profiles, again with different elemental, composite, and coated materials. The analysis of this simulation is ongoing.

Contents

1 Introduction/Background

1.1 Introduction

The purpose of this project is to use simulations to characterise the scattering of low-energy charged particle beams off flat material surfaces and to use the results of these simulations to inspire further simulations of tapered capillaries for low-energy charged particle beams. This project was completed as part of the 2023 CERN Summer Student Programme in collaboration with the BE-ABP Group at CERN. Much of the summer was spent developing the simulations (written in C++ and the `Geant4` framework) and establishing an effective workflow with batch job submissions through HT-Condor. The remaining time was spent writing analysis scripts in `Python` to characterise and plot the behaviours exhibited in the scattering and capillary simulations. Detailed outlines of the simulations and the corresponding analyses are found below.

1.2 `Geant4`

`Geant4` is the primary tool used for this research project, as it provides a widely used framework for the simulation of particle interactions with matter. `Geant4`, which stands for "Geometry and Tracking 4," is an open source software framework and is the successor of previous `GEANT` software toolkits developed by the `Geant4` Collaboration at CERN. It operates using object-oriented C++ programming and is used in many areas of physics research and development, not limited to high energy, nuclear, and accelerator physics.

`Geant4` uses a semi-classical approach to particle interactions with matter. This enables `Geant4` to realistically model the behaviour of particles as they traverse various materials while maintaining the quantum mechanic effects present in real interactions. The motion of particles is tracked and treated classically, with well-defined positions and momenta. This tracking accounts for the initial conditions of the particles, including their energy, direction, and starting positions. As particles advance through matter, they may interact in various ways, including but not limited to: electromagnetically, with ionisation and bremsstrahlung, or hadronically, with nuclear scattering and particle decay.

Although tracking of particles may be done classically, the interactions themselves rely on the Monte Carlo method. Instead of precisely predicting each interaction, `Geant4` uses random numbers to sample probability distributions associated with different interactions. This statistical sampling mimics the probabilistic nature of quantum mechanics, ensuring a realistic representation of particle behaviour and interactions while maintaining computational efficiency.

`Geant4` further divides a particle's trajectory into discrete steps, each step involving the calculation of the particle's new position and energy after any interactions. This stepwise propagation method enables `Geant4` to track the path and energy loss of particles as they traverse a material. Notably, `Geant4` considers both energy loss, such as ionisation, and scattering, which can alter a particle's direction and energy.

In addition to primary particle tracking, `Geant4` accounts for secondary particle production. These secondary particles and their behaviour are tracked in a manner similar to that of primary particles. Moreover, users can define detectors and scoring volumes within the simulation, allowing them to collect specific information about the final positions, energy deposits, or interactions of the particles, facilitating detailed analysis and interpretation of the simulation results.

1.3 Historical Tapered Capillary Results

Inspiration for this project stemmed from results obtained in 2007 and 2010 at the RIKEN-RAL muon facility and the TRIUMF M9B muon beamline, respectively, regarding the use of physical tapered capillaries for the enhancement of the density of low-energy muon beams.

The first study by Kojima et al. [3] demonstrated that a muon beam with a momentum of $54\,\mathrm{MeV}/c$ passing through a tapered glass tube can have its density increased by up to a factor of two, depending on the geometry of the tube. Historically, the use of spin-polarised muons for material science studies has been held back by the relatively large size of polarised muon beams (determined by the full width at half-maximum, FWHM, of the position distributions), which limits the size of the target material sample. At the RIKEN-RAL muon facility, Kojima et al. studied both μ^+ and μ^- beams passing through tapered Pyrex glass tubes with an input diameter of 46 mm, an outlet diameter in the range 3 mm to 20 mm (with lengths from 100 mm to 400 mm), and a thickness of 2 mm. For a fixed length of 400 mm, the enhancement of the

beam density has a monotonically decreasing relationship with the outlet diameter. As the capillary outlet diameter decreased from 20 mm to 5 mm, the beam density enhancement factor increased from ~ 1.5 to ~ 2.3. For a fixed capillary outlet diameter of 20 mm, the enhancement of beam density was found to have a monotonically increasing relationship with the capillary length. As the length increased from 100 mm to 400 mm, the beam density enhancement factor increased from ~ 1.0 to ~ 1.5. Furthermore, Kojima et al. simulated this density enhancement under vacuum conditions for μ^+ and μ^- beams with momenta varying from 27 MeV/c to 81 MeV/c. This simulation showed that a double in the beam density is nearly constant over the entire simulated momentum range. Their simulation also indicated that increasing the density of the capillary material may further increase the density enhancement achieved [3].

Based on the results of Ref. [3], a second study was performed at the TRIUMF M9B muon beamline. This study benefited from the ability of the TRIUMF facility to study detailed particle-by-particle behaviour using a continuous muon beam. In addition to the density factor as measured in the previous experiment, further beam kinematics (i.e. energy, beam profile, etc.) could be measured with this new experiment. Furthermore, as supported by the Monte Carlo simulation used in the previous study, Tomono et al. [5] used metal and glass capillaries with different profiles, tapering plates, trapezoidal tubes and conical tubes, for comparison. The TRIUMF beamline consists of positive muons (μ^+'s) in a momentum range of 30 MeV/c to 45 MeV/c. Before entering the tapering capillary, the beams pass through a lead collimator followed by a scintillator to define the input beam. Downstream of the capillary, three different configurations were used to characterise the output beam of muons.

This study provided a more comprehensive look at the effects of tapered capillaries on muon beams. The first results refer to the narrowing plates. Tomono et al. tested polished copper plates, rough copper plates, gold-plated copper plates, and glass plates, with the central momenta of the beam at 35 MeV/c and 45 MeV/c. The beam spectra recorded by a solid scintillation detector (SSD) 10 mm downstream of the capillary end indicated an increase in the density of the beam with the tapered plates and that the increased yield was mainly lower momenta muons, compared to a slit of the same output diameter. It is speculated that these lower momenta muons are those that are reflected off of the tapering plates and that they lose energy in the process. When comparing the plates with each other, it was observed that the density enhancement increased with the density of the material used, i.e., gold-plated copper plates yielded the highest density enhancement factor of 1.3, followed by copper and glass plates (with a central momentum of 35 MeV/c). No effect was observed as a result of the surface roughness of the plate materials. The SSD detector was moved from $-10°$ to $20°$. Most of the muons scattered between $-10°$ and $10°$, and very few muons scattered between $10°$ and $20°$ degrees (and those that did were of very low energy). Further downstream (100 mm), the beam width that had passed through the tapered plates was comparable to that of a slit with the same outlet width as the tapered plates, indicating that density enhancement comes at the cost of broadening of the angle spectrum of the beam.

Similar results were demonstrated with tapered tubes (trapezoidal and conical). Since these tubes focus the beam in both vertical and horizontal directions, the maximum density enhancement was observed to be 1.7 (with a central momentum of 40 MeV/c) for the trapezoidal copper tube (note that no gold-plated tubes were tested). Finally, the polarisation of the muon beam was compared at the outlet of the tapering tubes. The measurements were consistent within a standard deviation and no significant depolarisation of the muon beam was observed as a result of tapered capillaries [5].

Overall, this second study by Tomono et al. (2011) confirmed the preliminary results of Kojima et al. (2007). They conclude that the use of tapered capillaries can enhance the density of a muon beam by up to a factor of two, although this density is obtained close to the capillary exit and is therefore best used for fixed-target experiments. This density enhancement results from muon scattering at a small angle off of the capillary walls with small energy loss. Moreover, this density enhancement is greatest when the capillary is made of heavier elements.

The results from Refs. [3, 5] are the starting point for this research project, where we attempt to verify their findings through Geant4 simulations and to develop a more detailed understanding of the reflection process, which is suggested to lead to the observed density enhancement.

1.4 Beam Temperature/Cooling

A final piece to the background of this project is an understanding of beam temperature and cooling. This remains an aspect that was not tested by [3] or [5], but it may be of great importance to understand the potential uses of the tapered capillaries.

The temperature of a beam is split into two parts, the longitudinal beam temperature which is given by

$$\frac{1}{2}k_B T_\parallel = \frac{1}{2}mv_\parallel^2 = \frac{1}{2}mc^2\beta^2 p_\parallel^2$$

and the transverse beam temperature is given by

$$\frac{1}{2}k_B T_\perp = \frac{1}{2}mv_\perp^2 = \frac{1}{2}mc^2\beta^2\gamma^2\theta_\perp^2.$$

It is clear that the longitudinal beam temperature depends on the momentum distribution of the particle beam, while the transverse beam temperature depends on the angular distribution of the beam. It is important to note that beams can be anisotropic, i.e. the longitudinal and transverse temperatures are not equal.

In standard accelerator processes, the beam temperature is not reduced. In other words, standard accelerator processes generally abide by Liouville's Theorem (phase space density is conserved in a system controlled by external conservative forces) or they heat up the beam through residual gas, intrabeam scattering, etc. Beam cooling processes, however, break Liouville's Theorem.

Beam cooling is useful for many reasons. In particular, a cooled beam can improve luminosity and overall beam quality, it can compensate for beam heating factors, and it can increase the beam brightness [4]. For these reasons, studying whether tapered capillaries may have a beam cooling effect is of great interest.

2 Simulations

The first of the two main components of this project are simulations. These were written in C++ using the Geant4 framework.

For more information on the simulations, see Ref. [1].

2.1 Flat Scattering

The flat scattering simulation simulates the scattering of a low-energy particle off a flat surface. It records various information about the particle, including its initial momentum and incident angle, its scattered momentum and angle, whether it was transmitted, reflected, or absorbed by the flat plate, and more. All this information is recorded in an event tree in ROOT Ntuples. These data can then be used for analysis.

The simulation itself consists of a few distinct sections. There is a simulation.cc script which takes the input parameters of the simulation and passes them along to the other components, initialises all of the components, and sets the simulation in motion. Once the simulation has ended, the script is terminated. Aside from the simulation.cc script, there are three main components. The detector construction (i.e. the set up of the flat plate, its material, thickness, etc.), the action, which is comprised of four sub-parts (the run action, the event action, the step action, and the generator), and finally the physics list (which is typically a set of pre-packaged Geant4 physics interactions to be chosen for the energy range of concern) (see Fig. 1 for a dependency chart of these different components).

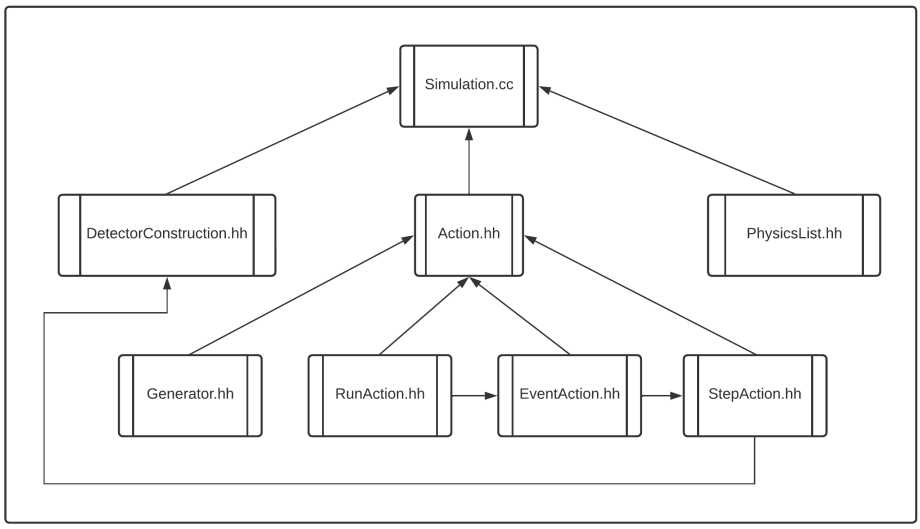

FIGURE 1: Dependency diagram of the flat scattering Geant4 simulation.

2.1.1 Simulation

At the core of this simulation is the simulation.cc script. This script takes command-line arguments to set numerous parameters (see Table 1).

TABLE 1: Command line arguments for simulation.cc

1	.mac file (determines visualization and number of events)
2	plate material (copper, gold-plated copper, glass, etc.)
3	beam angle (with respect to the normal)
4	beam momentum
5	particle type (e^-, μ^-, μ^+, p)
6	plate thickness
7	output file name
8	path to output file
9	visualisation (on/off)

The script then initialises the other three components of the simulation, the detector construction, the physics list, and the action. During this initialisation, the appropriate simulation parameters will be passed into their respective sections. Next, if enabled, the Geant4 GUI interface will be initialised (this is not used in batch simulations).

Once these initialisations are complete, the .mac file passed in to the script via the command line will be executed. A .mac file is a brief set of instructions that Geant4 uses to run a simulation. For this flat scattering simulation, the .mac files set up the GUI visualisation parameters (if enabled), the total number of events for the simulation to run, and the verbosity with which the simulation is run (for debugging purposes). Once all of these commands have been run to completion, the script will terminate.

2.1.2 Detector Construction

The physical world of the simulation is set up in the Detector Construction files. Although this simulation does not simulate a detector per se, this naming convention is standard for Geant4 programs.

First, the possible materials are defined. Geant4 has a library of standard elements, such as gold, copper, etc., that can be used as is. However, some composite materials, such as glass, must be constructed independently. For this simulation, the glass material is made up of 75% silica (SiO_2), 12% lime (CaO), and 13% soda (Na_2O). This is a typical composition of a former, stabiliser, and flux (respectively). All other relevant materials are taken from the Geant4 library.

The world and shapes are then constructed, each comprising a solid, logical, and physical component. First, we construct the simulation environment, i.e. the "world", which is a $8\,m^3$ cube comprised of a vacuum. Along the centre plane of this world, we construct the scattering plate with the desired thickness and material determined by the simulation.cc command line arguments. Finally, if there is a coating specified in the simulation arguments, we construct a third shape on top of the scattering plate with a fixed thickness (of 5 µm, which was the thickness of the gold plating used by [5]; different thicknesses were tested later on).

Lastly, for the purpose of visualisation alone, colours are associated with each of the constructed shapes.

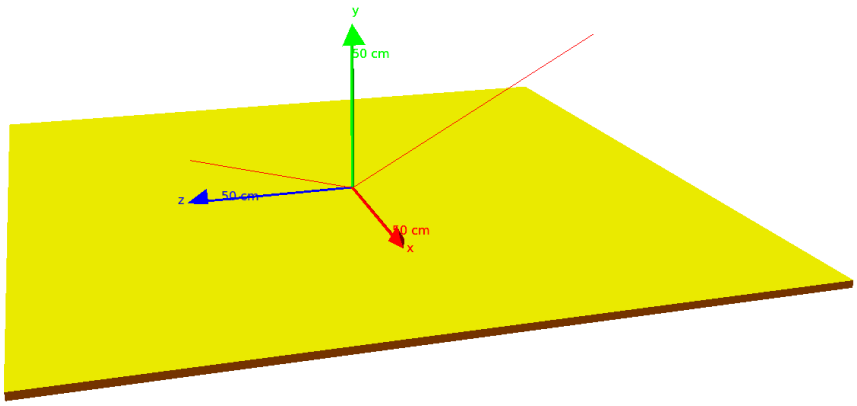

FIGURE 2: Image of the flat scattering simulation (with a gold plated copper plate). The particle is incident from the left and reflects to the right.

2.1.3 Physics List

The physics list is a small but important part of the simulation. Here, the allowed physics processes are declared. These can be manually programmed, although for the purposes of this simulation we use standard Geant4 physics processes. We use the Geant4 Electromagnetic Standard Physics package, which is equipped with all electromagnetic physics processes from the keV to PeV range, and the Geant4 Decay Physics package, which is equipped with electromagnetic decay processes (in case the simulation is expanded for a broader range of incident particles). Finally, we include the Geant4 Step Limiter Physics package, which allows the adjustment of the simulation step size.

2.1.4 Action

The action section of the simulation is fittingly where the bulk of the action takes place. Simply, the generator sets up the particle gun (i.e. the particle type, initial momenta, etc.), the run action generates individual events which comprise of a single particle scattering, the event action simulates these individual scattering events, and the step action implements the physics processes at each step in the event. The action script initialises the particle beam parameters (incident angle with respect to the plate normal, incident particle

momentum, and particle type) passed from the simulation command line arguments, as well as the output file name and path where the event data will be recorded. It creates instances of the generator, run action, event action, and step action, which start the simulation process.

Generator

The generator sets up a particle gun that lies on a sphere of radius 0.5 m centred at the origin. It has an incident angle determined with respect to the normal of the plate (i.e. 0° is perpendicular to the scattering plate and 90° is parallel to the plate surface) that is assigned as a simulation parameter. The beam momentum and particle type are also assigned to the particle gun, which is set to emit one particle per event.

Run Action

The run action oversees all of the events generated in the simulation. Its primary purpose is to set up the ROOT Ntuples where the event information will be stored and to save the ROOT file once all events have been completed. At the beginning of the run, two Ntuples are created: one for primary events (i.e., where no decay or absorption occurs) and one for all events. For primary events, the Ntuple columns are assigned for the event number, output momentum, and output angles. For all events, Ntuple columns are assigned for the event number and Boolean values that indicate whether the particle decayed (and if so, where) and whether the particle was absorbed by the plate. At the end of the run, the Ntuples are written to the ROOT output file and saved at the desired location.

Event Action

The event action concerns each individual particle scattering event. At the beginning of the event, output parameters (momentum components, Boolean decay/absorbed values, etc.) are initialised. As the scattering occurs, the step action will update these values as appropriate. At the end of the event, if the particle decayed or was absorbed, this was recorded in the appropriate Ntuple columns. If neither, then the particle was reflected or transmitted. The outgoing angles are computed from the outgoing momentum components, and both are recorded in their respective Ntuple columns.

Step Action

As each particle scattering event is simulated, the particle undergoes discrete steps through each physical material (as set up in the detector construction). At each vertex, appropriate physical processes are computed and update the particle's state. At each of these steps, we first record the particle PDG and current volume (i.e., in which material it is currently in). If the primary particle PDG does not agree with the incident particle, we conclude that the particle has decayed and assign the decay Boolean value to be true. We also record the new particle PDG, which can give insight into the type of process that led to the decay (currently this information is not used in the analysis). We then check whether the particle is entering the scattering plate. If the particle is not decayed when it takes its last step in the scattering plate, we record its three momenta. If the particle never leaves the plate, we conclude that it has been absorbed, and update the corresponding absorbed Boolean value to be true. Throughout this process, all of the event information is recorded. The event action will then add the recorded values to the appropriate columns of the ROOT Ntuple.

2.2 Tapered Capillaries

The tapered capillary study simulates a low-energy particle beam passing through a tapered capillary with an assigned profile. The incident beam is assigned an energy distribution, an angular distribution, a particle type, and a vertex distribution. The simulation records the angle and energy of the particles in the beam as they enter the tapered capillary and as they leave the tapered capillary. The simulation is set up to handle various capillary profiles: conical, hyperbolic, and parabolic.

The structure of the simulation is quite similar to that of the flat-scattering simulation. There is a simulation.cc script which takes the input parameters of the simulation and passes them along to the other components, initialises all of the components, and sets the simulation in motion. Once the simulation has ended, the script is terminated. Aside from the simulation.cc script, there are three main components. The detector construction (i.e. the set up of the flat plate, its material, thickness, etc.), the action, which is comprised of four sub-parts (the run action, the event action, the step action, and the generator), and finally the physics list (see Fig. 3 for a dependency chart of these different components).

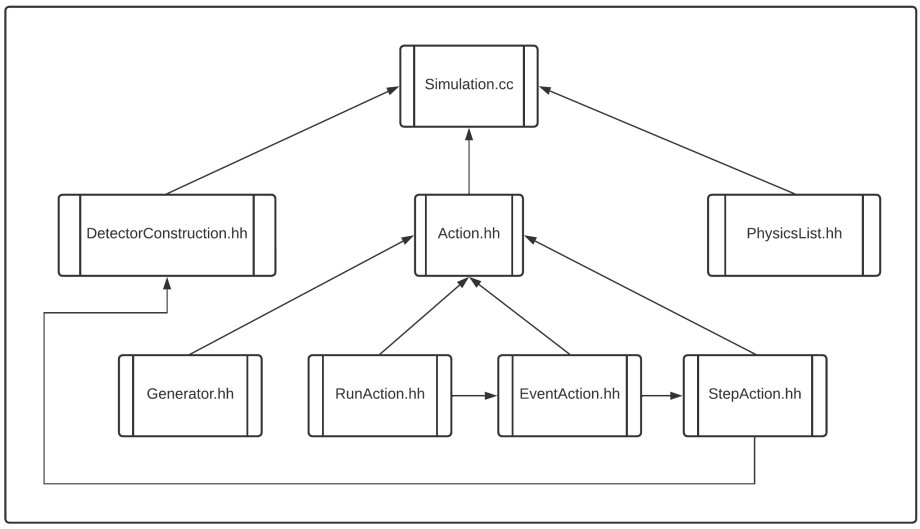

FIGURE 3: Dependency diagram of the tapered capillary Geant4 simulation.

The development of this tapered capillary simulation is ongoing, so there may be components that are incomplete. The overall structure is completed, but the output data may not necessarily contain what is in the final simulation.

2.2.1 Simulation

The simulation.cc script, which initialises the simulation (and GUI if enabled), is nearly identical to the corresponding script for the flat scattering simulation. The primary difference is the input parameters for the simulation (see Table 2) and that this script configures the particle source instead of the generator file (a quirk of Geant4's non-point source particle beams).

TABLE 2: Command line arguments for simulation.cc

1	.mac file (determines visualisation and number of events)
2	capillary material (copper, gold-plated copper, glass, etc.)
3	capillary profile (conical, hyperbolic, parabolic)
4	capillary configuration (start and end radii, length, thickness)
5	output file name
6	output file path
7	visualisation (on/off)
8	particle type ($e^-, \mu^-.\mu^+, p$)
9	beam radius
10	beam vertex distribution (position standard deviation)
11	beam angle distribution (angle standard deviation)
12	beam energy

The detector construction, physics list, and action are initialised (and the GUI, if it is enabled), and the corresponding parameters are passed to each of these sections. The .mac file is executed just as in the flat scattering simulation, and once the events are complete, the script terminates. However, before the .mac file is executed, the beam parameters are passed as arguments into the Geant4 UI manager to properly configure the particle beam. The beam is centred at the origin and aligned along the axis of the tapered capillary.

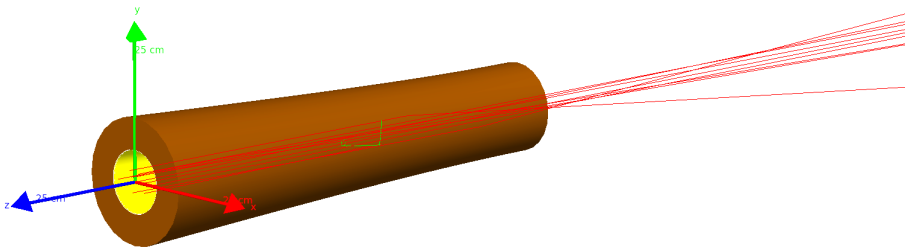

FIGURE 4: Image of the tapered capillary simulation (with a gold plated parabolic profile capillary). Particle beam passes from left to right through the capillary.

2.2.2 Detector Construction

The materials used for the detector construction are the same as in the flat scattering simulation. The primary difference in the detector construction is that we simulate tapered capillaries with a specific profile, rather than a flat plate.

The tapered capillaries are made up of polycone solids, a feature in Geant4 that produces a discretised solid of revolution, given arrays of inner and outer radii. Solid polycone works as follows: first, assign an array of z values $[z_1, \ldots, z_n]$ for some large n where $z_1 - z_n$ is the desired length of the capillary; next, determine the profile function of the capillary, i.e., $p(z)$, and the desired thickness of the capillary, say $h > 0$; compute the corresponding arrays $[p(z_1), \ldots, p(z_n)]$ and $[p(z_1) + h, \ldots, p(z_n) + h]$ which give the inner and outer radii of the capillary for each slice z_i, respectively. These arrays are passed to the Geant4 polycone function, which produces a solid formed by connecting washers at each vertical slice z_i (with inner radius $p(z_i)$ and outer radius $p(z_i) + h$) with conical sections. The larger the number of vertical slices n, the closer the simulated capillary is to a smooth solid of revolution.

The types of profiles implemented in this simulation include conical sections (formed by straight line profiles)

$$C(z) \in \{f : [0, L] \to \mathbb{R} | f(z) = az + b, \quad a, b \in \mathbb{R}\};$$

hyperbolic sections

$$H(z) \in \left\{ f : [0, L] \to \mathbb{R} \middle| f(z) = R\sqrt{1 + \left(\left(\frac{r}{R}\right)^2 - 1\right)\left(\frac{z}{L}\right)^2} + h, \quad r, R, L, h > 0, \quad R > r \right\}$$

where R is the entrance radius, r is the exit radius, L is the length of the capillary, and h is a vertical offset; and parabolic sections

$$P(z) \in \left\{ f : [0, L] \to \mathbb{R} \middle| f(z) = R + (r - R)\left(\frac{z}{L}\right)^p + h, \quad r, R, L, h > 0, \quad R > r, \quad p \in \mathbb{N} \right\}$$

where R is the entrance radius, r is the exit radius, L is the length of the capillary, h is a vertical offset, and n is the order of the polynomial.

To add a coating to the interior of the capillary, we replace a fixed thickness (set to 5 µm) of the innermost section of the capillary with a different coating material. The process of generating the shape of the coating is the same as that of generating the initial capillary.

In addition to the physical capillaries, we added two fictitious thin disks at the entrance and exit of the capillary. They have no physical interaction with the simulated particles; however, they enable verification of when particles are entering and leaving the capillary, so that we can record particle information exactly when they enter and exit the capillary.

2.2.3 Physics List

Since this simulation concerns the same interactions as the flat scattering simulation, the same Geant4 physics process packages are used.

2.2.4 Action

The action, run action, event action, and step action follow the same procedures as in the flat scattering simulation. This part of the tapered capillary simulation is still a work in progress, as it has not yet been decided what particle/event information is important to record for analysis purposes.

Generator
As noted above, the setup of the particle beam is done primarily in the simulation.cc script for this simulation (which is different compared to the flat scattering simulation). As a result, the generator file serves only to initialise each event, this time with a general particle source instead of a particle gun.

3 Analysis/Results

3.1 Flat Scattering

With the flat-scattering simulation complete, batches of simulations were run and data analysis was performed to characterise the scattering. The batch system is the HT-Condor and CERN lxplus. The details of the batch workflow and explanations for how to run the simulations can be found in Ref. [1], the next step was to write an analysis script to plot and fit the scattering data for various particle, angle, momentum, and plate material configurations.

3.1.1 Analysis Script

The primary analysis script is written in Python and makes use of numpy and scipy for data analysis, uproot to extract data from ROOT Ntuples, and matplotlib to produce plots and histograms.

The general structure of the analysis script is as follows:

1. An analysis setup file is read, which specifies what type of plots are to be made, and which ranges of particles, momenta, incident angles, and plate materials are included in the data.
2. Next, the data files corresponding to the specifications in the configuration file are read from some specified database where the simulation output data were recorded.
3. Nested iteration is performed over the particle type, plate material, incident momentum, and incident angle (from outer to inner loops) of the simulated data.
4. For each incident angle (with fixed particle type, plate material, and momentum), the number of transmitted, reflected, absorbed, and decayed particles is recorded, along with the outgoing angles and momenta.
5. These outgoing angle and momentum data sets are binned (using numpy's auto histogram binning). We then compute the mean, mode, standard deviation, mean error, and mode error of these histograms. The mean and standard deviations are computed as normal for discrete data sets. The mean error is calculated as the standard error on the mean (SEM)

$$SEM = \frac{\sigma}{\sqrt{N}}$$

where σ is the standard deviation and N is the size of the data set (this will later be changed to root mean squared error). The mode is more difficult to compute. Initially, attempts were made to fit the distributions to asymmetric bounded probability distributions (such as a beta distribution). However, these attempts failed for large incident angles (i.e., angles close to the scattering plate). The chi-squared / dof values were calculated and confirmed that the attempted fits did not agree with the

histograms. Instead, numpy.random.choice is used to take 100 random samples of the data, normalised to the full data set size, which are then binned using the same numpy auto histogram binning. Then, using this binning, the mode is computed as the centre of the maximum bin (this works well, so long as the distributions being used are unimodal). Doing this 100 times provides a series of mode measurements from which the mean-mode determination and the standard error on this mean can be computed. These are taken to be the mode and mode error of the data distributions. This method, while it does converge relatively well, will be replaced by a more well-founded algorithm in the future.

6. The mode, mean, standard deviation, mean error and mode error are then appended to the arrays for each momentum, providing distributions of these parameters for fixed particle type, plate material and incident momentum over the entire range of incident angles.

7. The number of reflected, decayed (split into decayed before the particle-plate interaction and decayed after the particle-plate interaction), and absorbed particles per fixed incident angle is added to the arrays for each momentum. This similarly provides distributions of these parameters for fixed particle type, plate material, and incident momentum over the entire range of incident angles.

The remainder of the analysis script consists of plotting these distributions and parameters in various different configurations as will be shown in later sections of this report. All of the plots below, and many more, are available at [1].

3.1.2 Muon Angle and Momentum Study

One of the first studies performed was a brief analysis of the momentum and angular distributions of the reflected μ^-s. Histogram arrays were produced for incident momenta of $30\,\mathrm{MeV}/c$, $50\,\mathrm{MeV}/c$, $100\,\mathrm{MeV}/c$, and $200\,\mathrm{MeV}/c$, and incident angles of $20°$, $40°$, $60°$, and $80°$ with respect to the normal of the scattering plate (see Figs. 5 and 6 for the case of a 5 mm thick gold-plated copper scattering plate).

It was observed that there is a noticeable drop in the number of reflected particles for low angles and higher momenta. Moreover, the lower the incident momentum and the lower the angle, the closer the mode of the reflected momentum distribution to the incident momentum. For the reflected angle θ, it was observed that the mode of distribution of the reflected angles is more in agreement with the incident angle at higher energies (at large angles). For low angles, the distributions have very few entries, so there is not much to say about them. We notice that for low angles and high energies, there are some configurations in which no reflection occurs. These general trends were also visible for the case of a copper scattering plate and a glass scattering plate (with a 5 mm thickness).

This initial study indicated that more reflection is achieved at larger incident angles, and while higher incident momentum may keep the reflected angle mode closer to the incident angle, there a greater loss in momentum occurs.

3.1.3 Initial Reflection/Transmission Study

As noted above, there were certain simulation configurations with high incident momentum and low incident angle where no reflection was observed. To understand what is happening to these particles, a follow-up study was conducted to check the behaviour of all of the particles in the simulation and assess whether they are reflected, transmitted, absorbed, or decay to other particles at some step in the simulation.

It was observed that the number of reflected particles peaks for large incident angles, regardless of the incident momentum. For muons that scatter off a copper plate, this peak reaches its largest value between $30\,\mathrm{MeV}/c$ and $90\,\mathrm{MeV}/c$, although it remains fairly constant throughout the momentum space. For low incident momentum and incident angles below $70°$, most of the muons are absorbed by the copper plate. As the incident momentum increases, starting from the lowest incident angle, most muons begin to transmit through the plate instead of being absorbed. Intuitively, this progression from the lowest angles increasing to higher angles as the incident momentum increases makes sense because the effective cross section of the plate is larger for larger incident angles. Eventually, the number of reflected muons over the whole range becomes smaller as the incident momentum increases, although all of the remaining reflection continues to occur at large incident angles only.

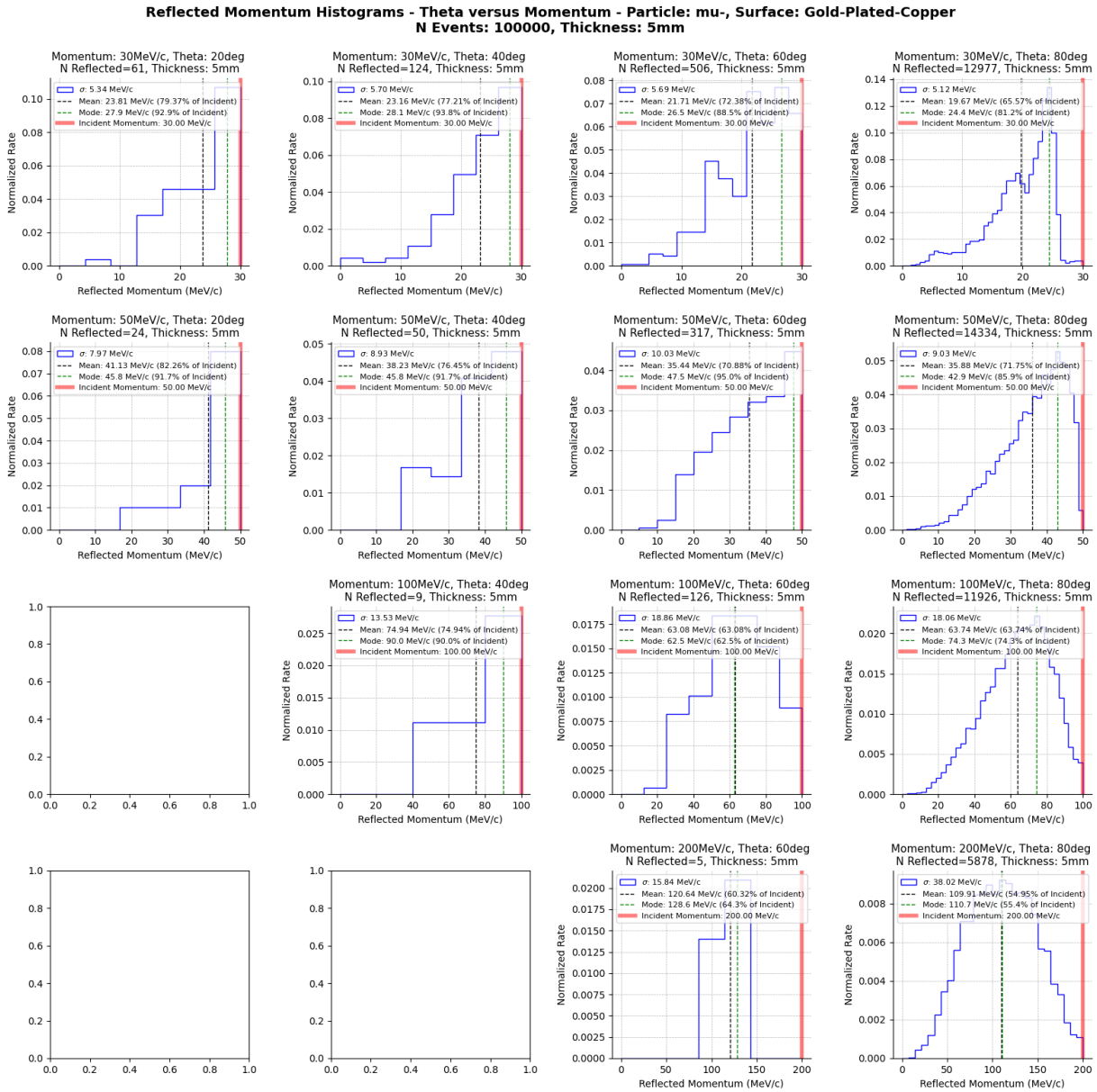

FIGURE 5: Array of histograms of the reflected momentum of μ^- reflecting off of a 5 mm thick gold-plated copper scattering plate. The histograms are arranged with increasing incident angle from left to right, and increasing incident momentum from top to bottom.

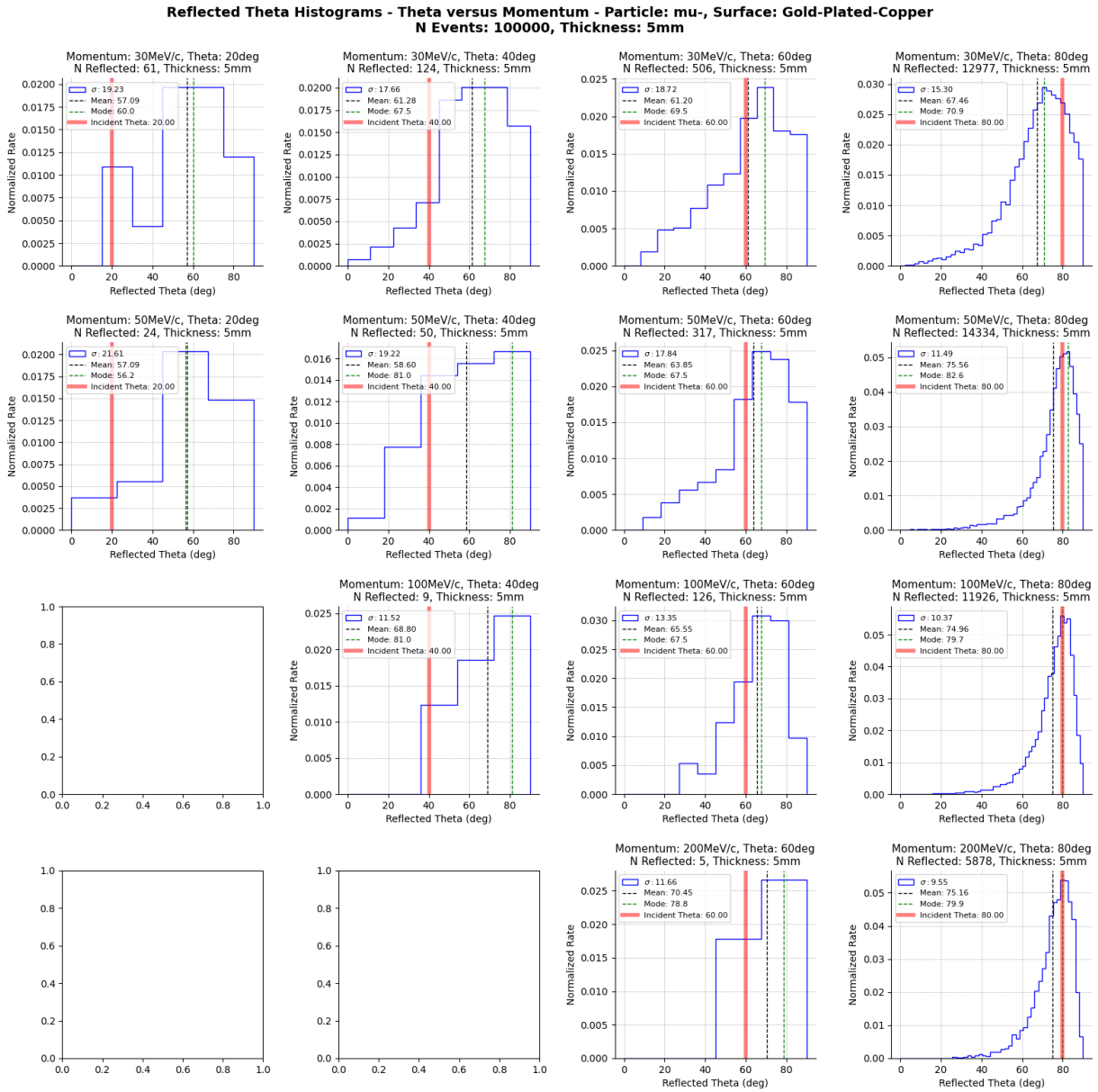

FIGURE 6: Array of histograms of the reflected angle of μ^- reflecting off of a 5 mm thick gold-plated copper scattering plate. The histograms are arranged with increasing incident angle from left to right, and increasing incident momentum from top to bottom.

Another important note is that it appears that no muons decay before reaching the scattering plate. This means that the particle gun in the Geant4 simulation is set at an appropriate distance from the scattering plate. If it was too far, we may lose out on data because muons could decay before interacting with the plate. It is also clear that the reflected and transmitted decayed muon counts follow a similar shape as the nondecayed reflected and transmitted muons (although there is much more noise because the number of decayed muons is significantly outweight by the nondecayed muons).

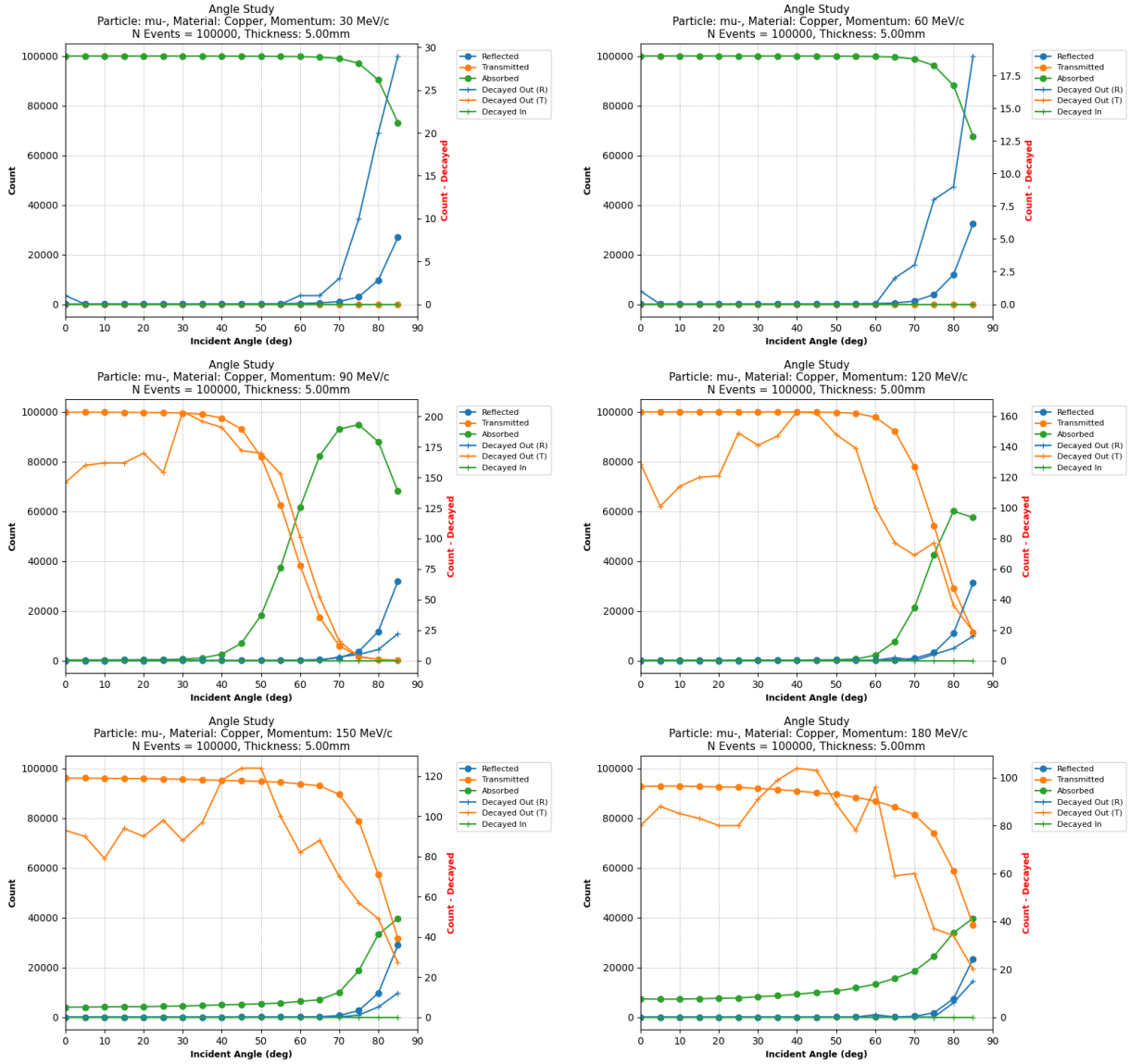

FIGURE 7: Plots of the counts of reflected, transmitted, absorbed, and decayed μ^- with a copper scattering plate over the whole range of incident angles $(0°, 90°)$, at incident momentum ranging from $30\,\mathrm{MeV}/c$ to $150\,\mathrm{MeV}/c$. Decayed In means that the particle decays before scattering, Decayed Out (T) means that it decayed after transmission, and Decayed Out (R) means that it decayed after reflection.

Similar plots were made for configurations with muons and glass and muons and gold-plated copper. Gold-plated copper exhibited behaviour nearly identical to that of the copper plate. The glass plate showed similar behaviour, although notable reflection started at lower incident angles. However, at large incident angles, the reflection rate was lower than that of the copper plate configuration (indicating a trade-off of sorts between copper and glass).

In addition, this study was performed with electrons and protons as well. For these configurations, it was observed that at a sufficiently low incident momentum, there was notable reflection across the entire range of angles (although this reflection still remained peaked at high incident angles). For electrons, the peak at high incident angles was more prominent than that of the proton, which exhibited the flattest reflection curve of all particles (see Fig. 8).

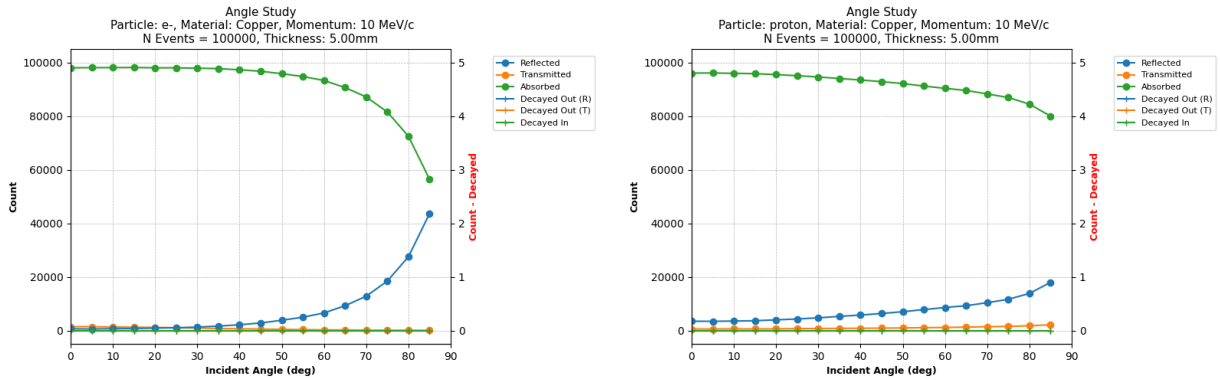

FIGURE 8: Plots of the counts of reflected, transmitted, absorbed, and decayed e^- (left) and p (right) with a copper scattering plate over the whole range of incident angles $(0°, 90°)$, at an incident momentum of $10\,\mathrm{MeV}/c$.

3.1.4 Cutoff Incident Angle Study

In the previous study, there was an indication that some configurations exhibit a lower incident angle where notable reflection begins to occur, whereas some configurations exhibit a higher rate of reflection at high incident angles. For this study, the cutoff angle was plotted against the incident momentum for a number of configurations to better observe this expected behaviour. The cutoff is defined as the smallest incident angle for which 1% of the incident particles were reflected.

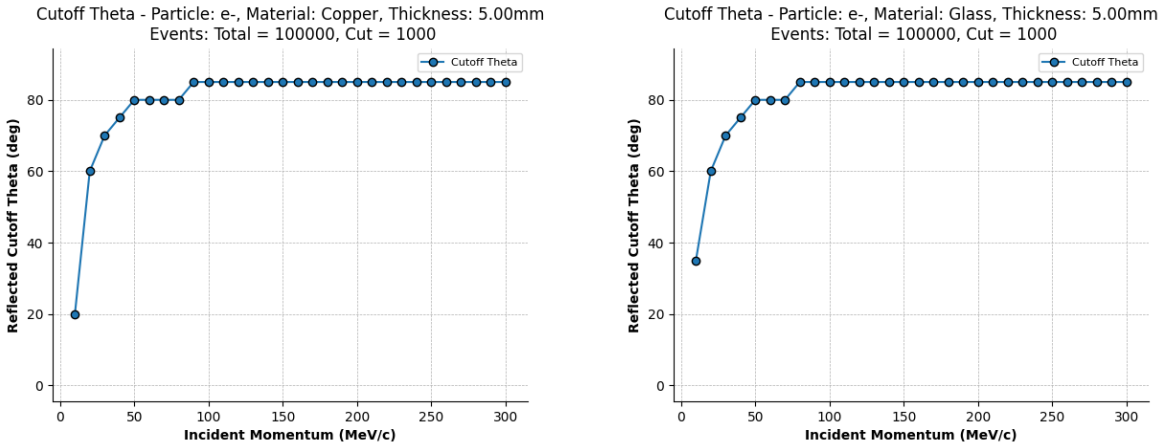

FIGURE 9: Plot of the cutoff angle versus incident momentum of e^- for copper (left) and glass (right) scattering plates.

It is clear from Figs. 9, 10, and 11 that electrons and protons exhibit a sharper increase in the cutoff angle as the incident momentum increases. Moreover, both protons and electrons appear to have a minimum cutoff angle for very low incident momentum (i.e. $10\,\mathrm{MeV}/c$ or less). On the other hand, the muon cutoff angles have a local minimum for a higher incident momentum (around $50\,\mathrm{MeV}/c$ for copper and similar for glass), and the change in cutoff angle per increment of incident momentum is much smaller than for electrons and protons.

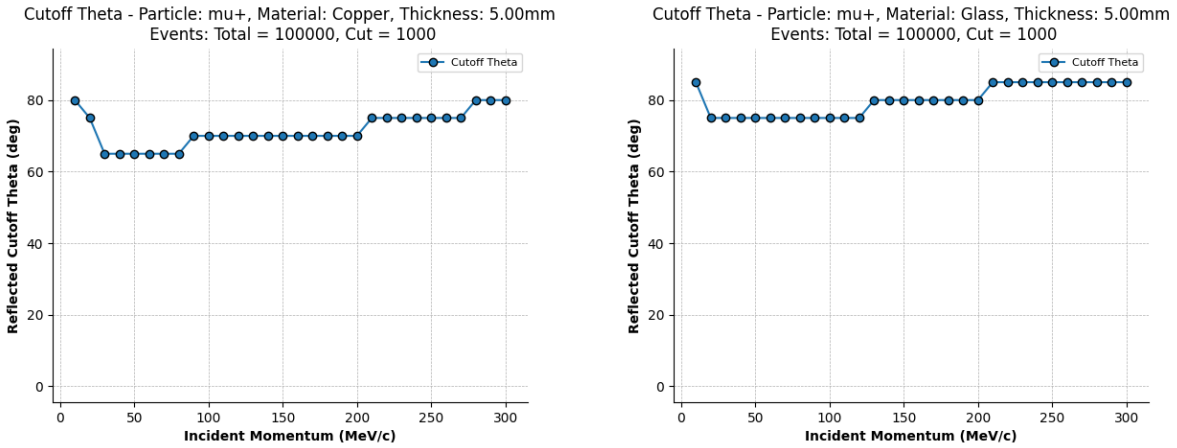

FIGURE 10: Plot of the cutoff angle versus incident momentum of m^+ for copper (left) and glass (right) scattering plates.

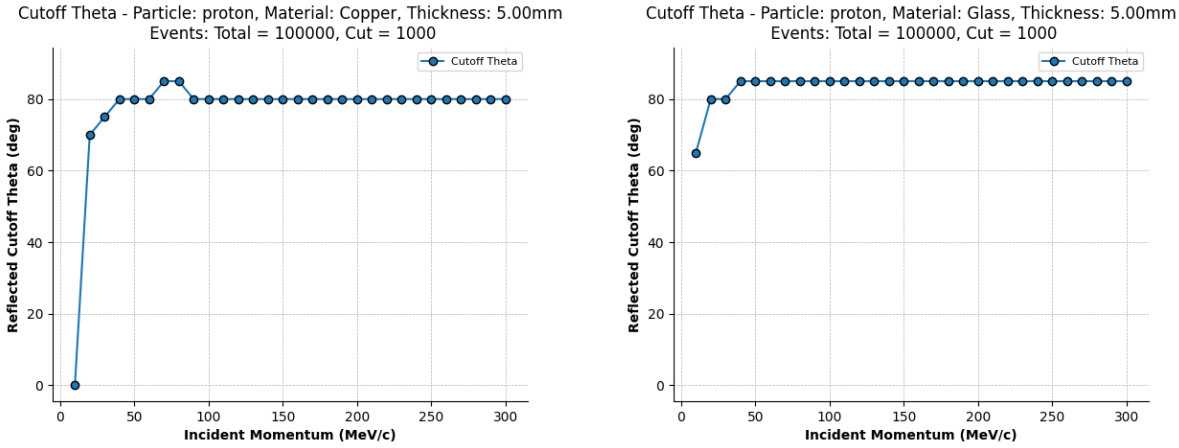

FIGURE 11: Plot of the cutoff angle versus incident momentum of p for copper (left) and glass (right) scattering plates.

3.1.5 Plate Thickness Study

Given the nature of this simulation, it is intuitive that decreasing the thickness of the plate should primarily result in an increase of the number of transmitted particles since the effective cross section of the particles through the plate is smaller. To verify that this is indeed the case, copper, glass, and gold-plated copper plates were tested with a muon beam at $80\,\mathrm{MeV}/c$. The results were as expected (see Fig. 12). As the thickness of the plate decreased, the number of particles transmitted increased, especially at high incident angles where there was originally less transmission.

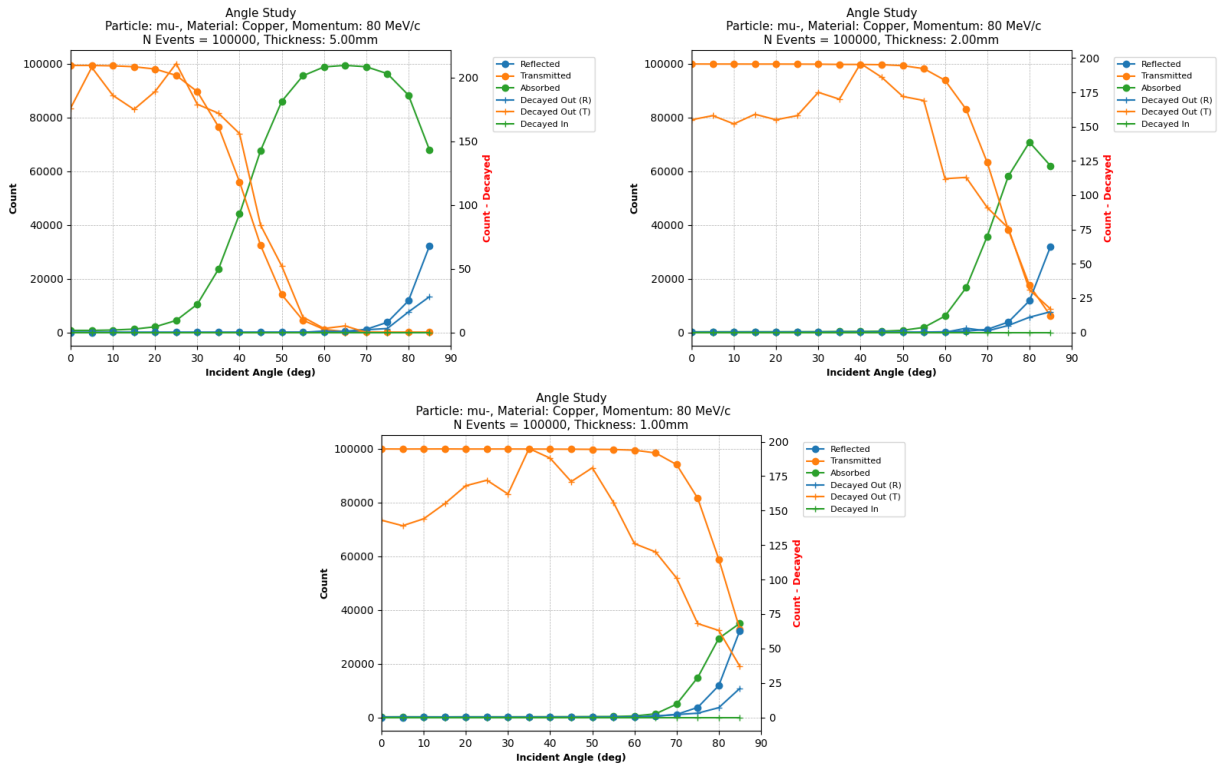

FIGURE 12: Plots of the counts of reflected, transmitted, absorbed, and decayed μ^- with a copper scattering plate over the whole range of incident angles $(0°, 90°)$, at an incident momentum of $80\,\mathrm{MeV}/c$. The upper left has a plate thickness of 5 mm, the upper right has thickness 2 mm, and the bottom has thickness 1 mm.

3.1.6 Higher Momentum Proton Study

It was observed that protons have interesting behaviours with a higher incident momentum. In previous studies, it was observed that as the incident momentum of the particle increased, the transmission rate increased, especially for low incident angles. However, as the incident momentum of protons increased into the GeV range, it was observed that this transition from having only transmitted particles and no absorbed particles was to some extent reversed (see Fig. 13). This may be an interesting artefact of the simulation or perhaps is indicative of some interesting and unexpected behaviour of higher-energy (with respect to this study) protons.

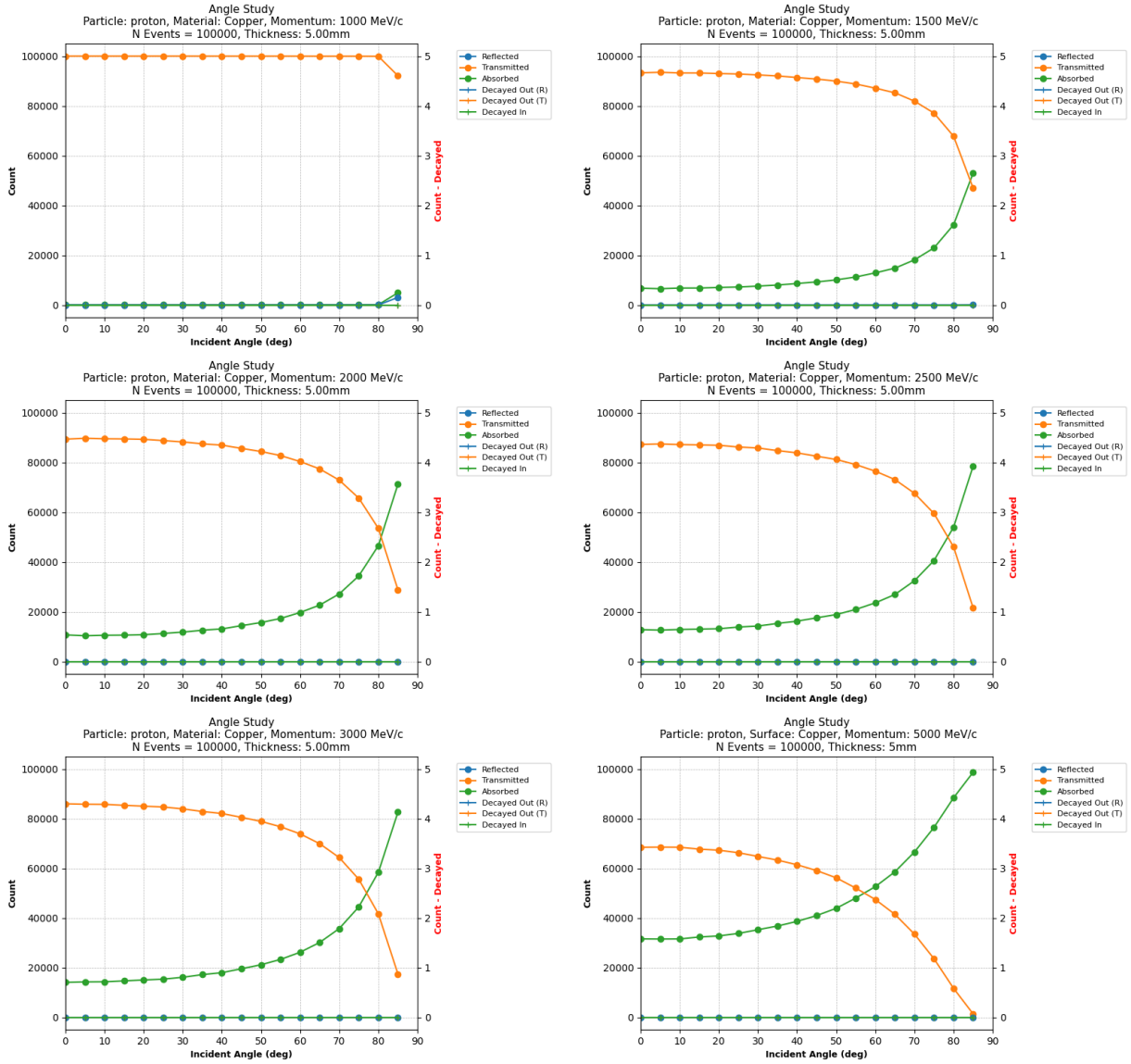

FIGURE 13: Plots of the counts of reflected, transmitted, absorbed p with a copper scattering plate (5 mm thickness) over the whole range of incident angles $(0°, 90°)$, at an incident momentum from 1000 MeV/c to 5000 MeV/c.

Increasing the thickness of the scattering plate to 10 mm, 15 mm, and 20 mm was also tested under these circumstances. As one might expect, this transition back to some amount of absorption instead of all transmission decreased in incident momentum as the plate thickness increased. Again, this may be explained by the increased thickness increasing the effective cross section of the plate for the incident particles.

3.1.7 μ^- and μ^+ Comparison Study

Similarly to the plate thickness study, intuition would suggest that positive and negative muons exhibit the same reflection/transmission behaviour. Nevertheless, a comparison between their behaviour is worthwhile to verify whether the simulation indicates any notable differences in their behaviour.

In Fig. 14 it appears that both positive and negatively charged muons exhibit similar behaviour, although there may be a slight difference in cutoff angle at low incident angles. Otherwise, the plots agree.

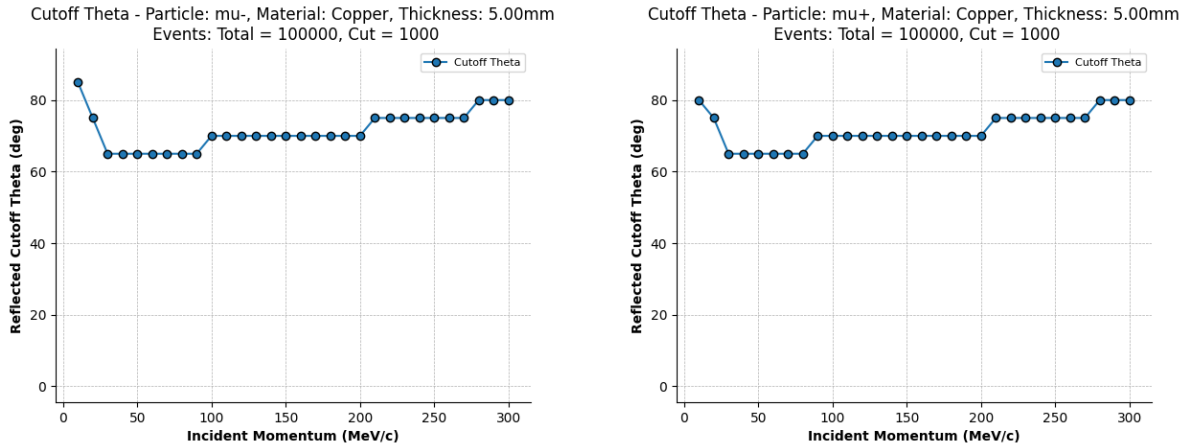

FIGURE 14: Cutoff incident angle plots for μ^- (left) and μ^+ (right).

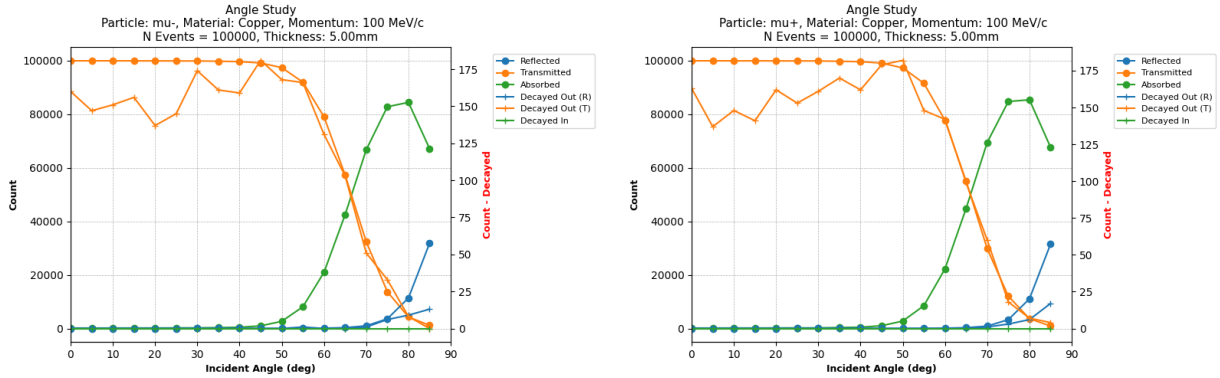

FIGURE 15: Plots of the counts of reflected, transmitted, absorbed, and decayed μ^- (left) and μ^+ (right) with a copper scattering plate (5 mm thickness) over the whole range of incident angles $(0°, 90°)$, at an incident momentum of 100 MeV/c.

Similarly, in Fig. 15, it appears that both positive and negatively charged muons exhibit very similar reflection, absorption, transmission, and decay behaviour. This was also checked for an entire range of incident momenta (10 MeV/c to 250 MeV/c), and the agreement persists throughout the range.

Although a further quantitative comparison between positive and negatively charged muons may be necessary to establish any minor differences, it is evident that the differences, if any, are quite minor.

3.1.8 28 MeV/c and 125 MeV/c μ^- Studies

From previous studies, good intuition has been developed regarding the behaviour of low-energy particle scattering off of flat surfaces. Now, we consider two incident momenta of interest: 28 MeV/c and 125 MeV/c as these momenta will be used for the proposed muon EDM experiment at PSI [2]. For this study, we also expanded the number of plate materials used: copper, glass, gold-plated copper, gold, aluminium, brass, bronze, iron, and stainless steel. This provides a good variety of material densities that may provide different scattering behaviour. Below are plots of the means and modes of the reflected-angle distributions versus incident momentum, the same reflection, transmission, absorption, and decay plots as seen in the previous studies, and 2D histograms of the reflected-momentum distributions versus incident angle. These provide a relatively complete characterisation of the scattering (and, notably, reflection) behaviour of low-momentum muons scattering off of flat material surfaces. Of the materials, glass, copper, and gold-plated copper are shown below. The plots of the other materials are shown in the Appendix.

Copper

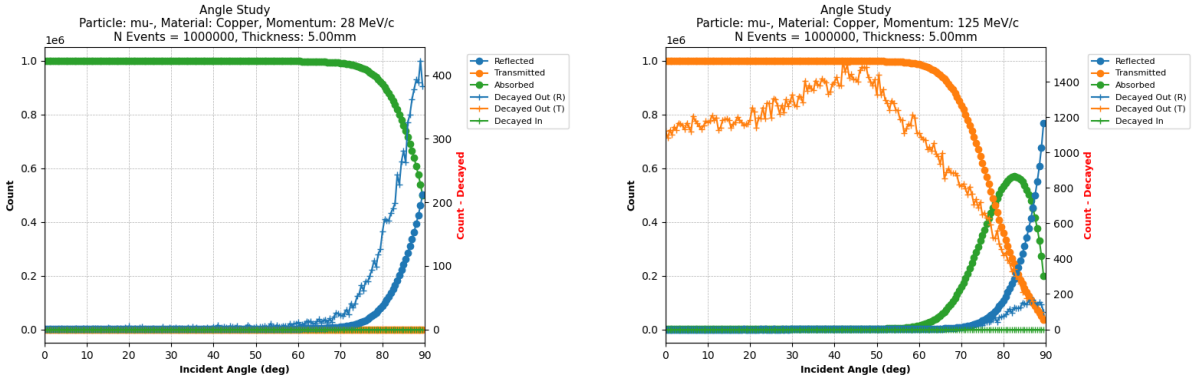

FIGURE 16: Plots of the counts of reflected, transmitted, absorbed, and decayed μ^- with a copper scattering plate over the whole range of incident angles $(0°, 90°)$, at incident momenta of $28\,\mathrm{MeV}/c$ (left) and $125\,\mathrm{MeV}/c$ (right).

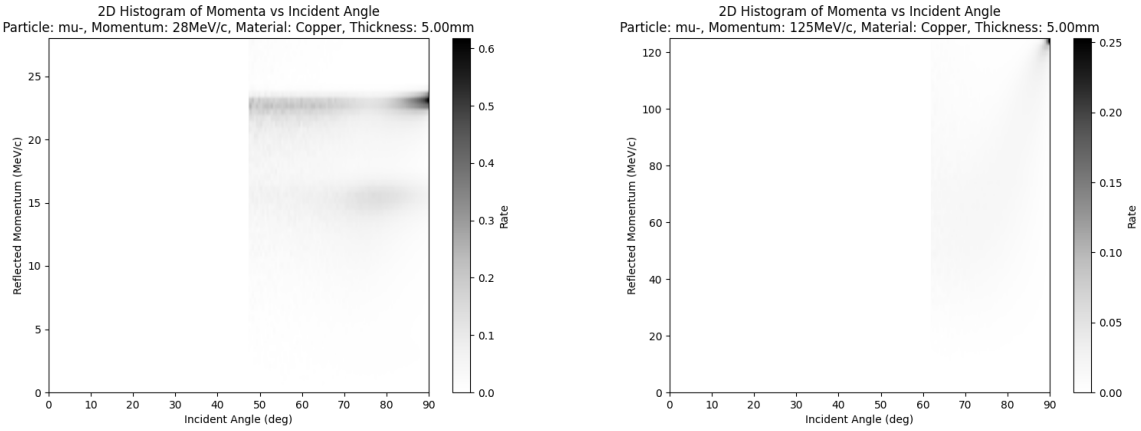

FIGURE 17: 2D histograms of the reflected momentum distributions (in a range where there is notable reflection) of μ^- reflecting off of a copper plate, at incident momenta of $28\,\mathrm{MeV}/c$ (left) and $125\,\mathrm{MeV}/c$ (right).

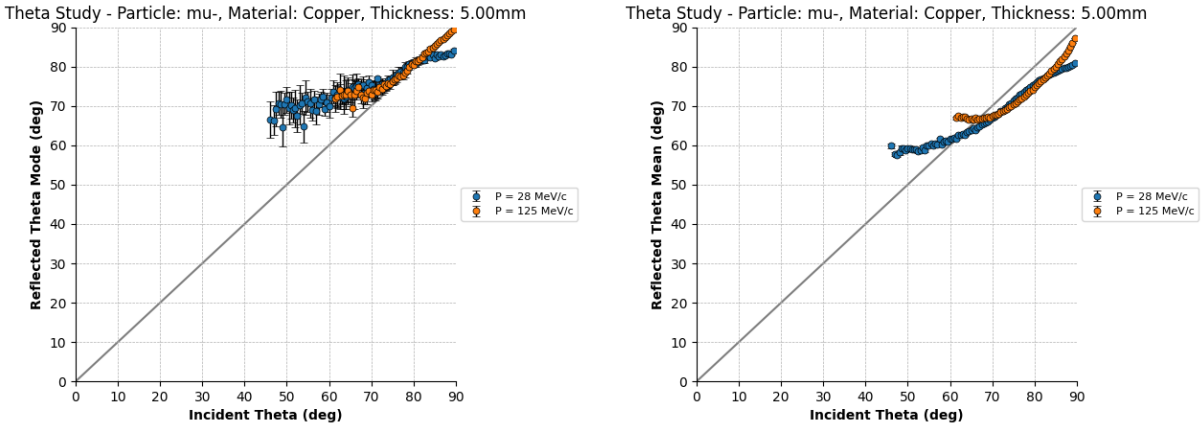

FIGURE 18: Plots of the mode (left) and mean (right) of the reflected angle distributions (in a range where there is notable reflection) of μ^- reflecting off of a copper plate, at an incident momentum of 28 MeV/c and 125 MeV/c.

Glass

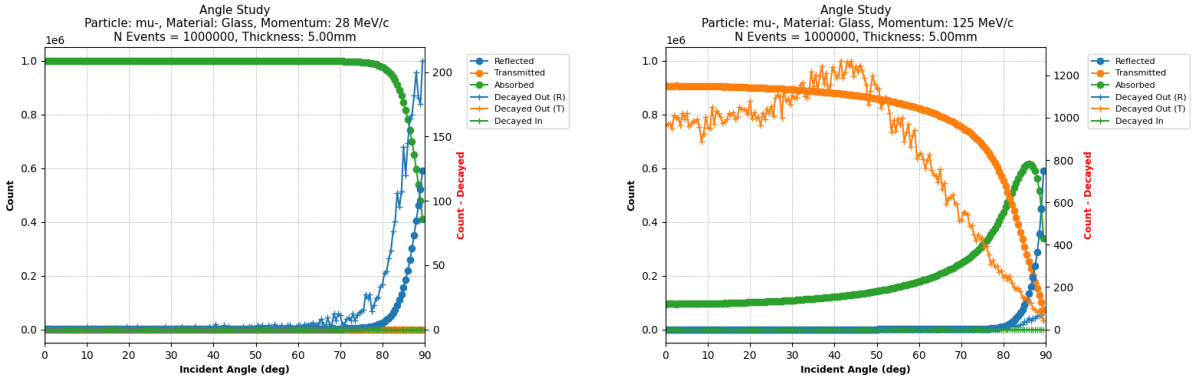

FIGURE 19: Plots of the counts of reflected, transmitted, absorbed, and decayed μ^- with a glass scattering plate over the whole range of incident angles $(0°, 90°)$, at incident momenta of 28 MeV/c (left) and 125 MeV/c (right).

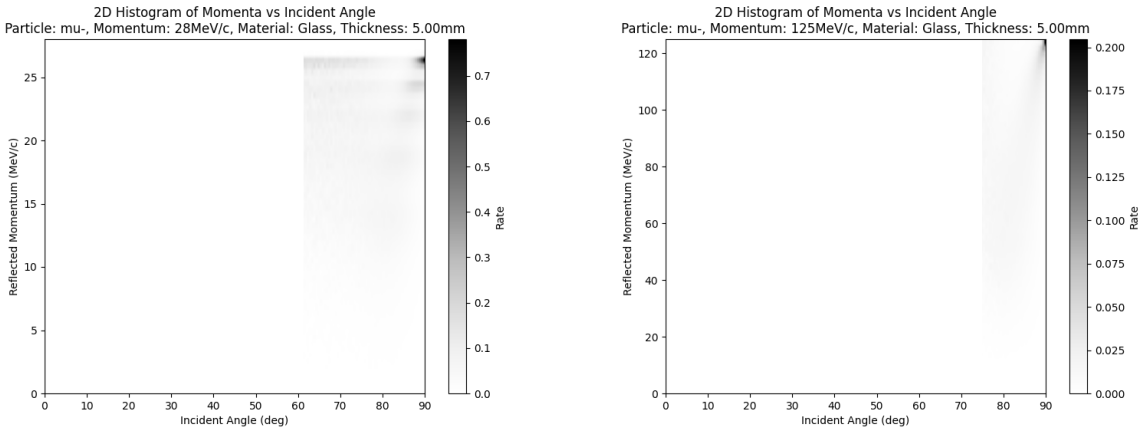

FIGURE 20: 2D histograms of the reflected momentum distributions (in a range where there is notable reflection) of μ^- reflecting off of a glass plate, at incident momenta of 28 MeV/c (left) and 125 MeV/c (right).

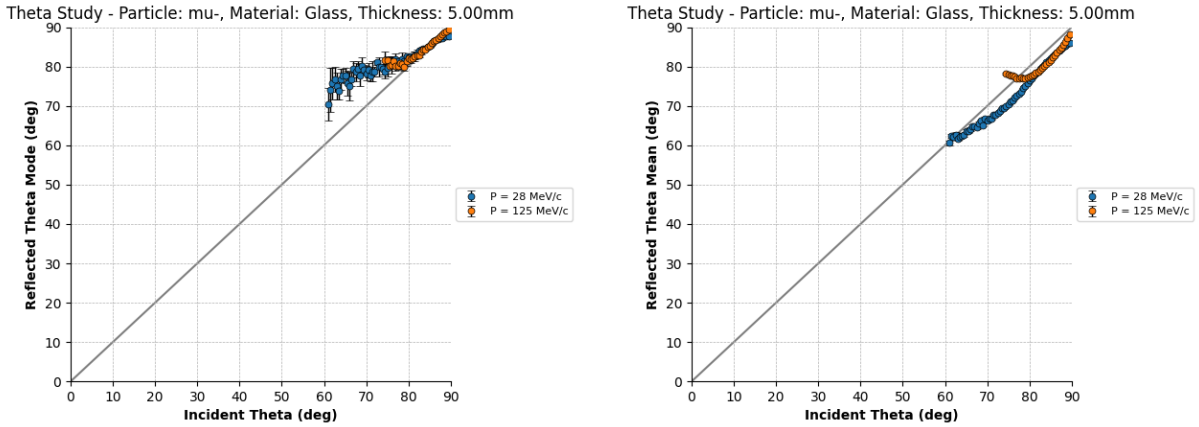

FIGURE 21: Plots of the mode (left) and mean (right) of the reflected angle distributions (in a range where there is notable reflection) of μ^- reflecting off of a glass plate, at an incident momentum of $28\,\mathrm{MeV}/c$ and $125\,\mathrm{MeV}/c$.

Gold-Plated Copper

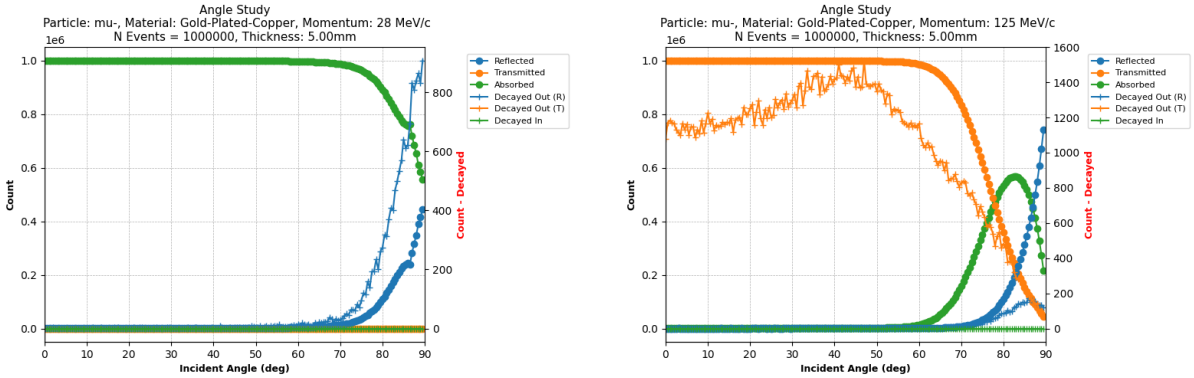

FIGURE 22: Plots of the counts of reflected, transmitted, absorbed, and decayed μ^- with a gold-plated copper scattering plate over the whole range of incident angles $(0^\circ, 90^\circ)$, at incident momenta of $28\,\mathrm{MeV}/c$ (left) and $125\,\mathrm{MeV}/c$ (right).

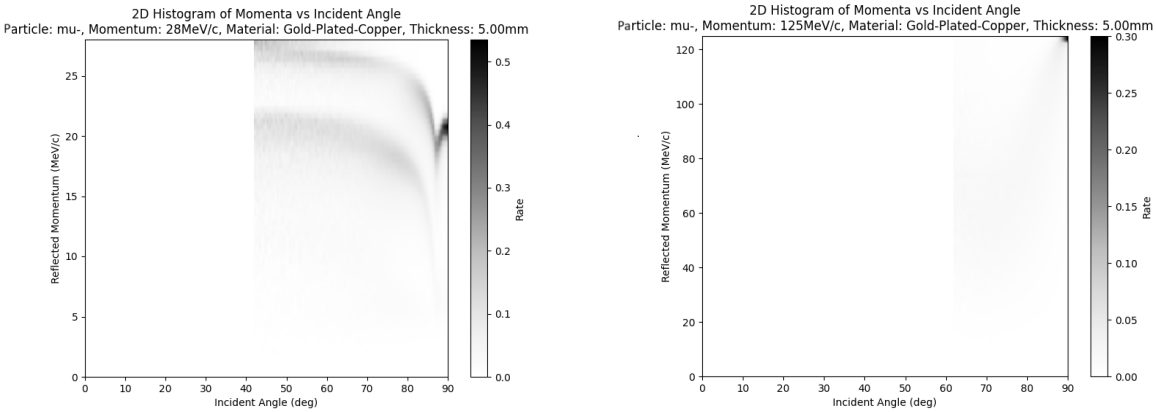

FIGURE 23: 2D histograms of the reflected momentum distributions (in a range where there is notable reflection) of μ^- reflecting off of a gold-plated copper plate, at incident momenta of $28\,\mathrm{MeV}/c$ (left) and $125\,\mathrm{MeV}/c$ (right).

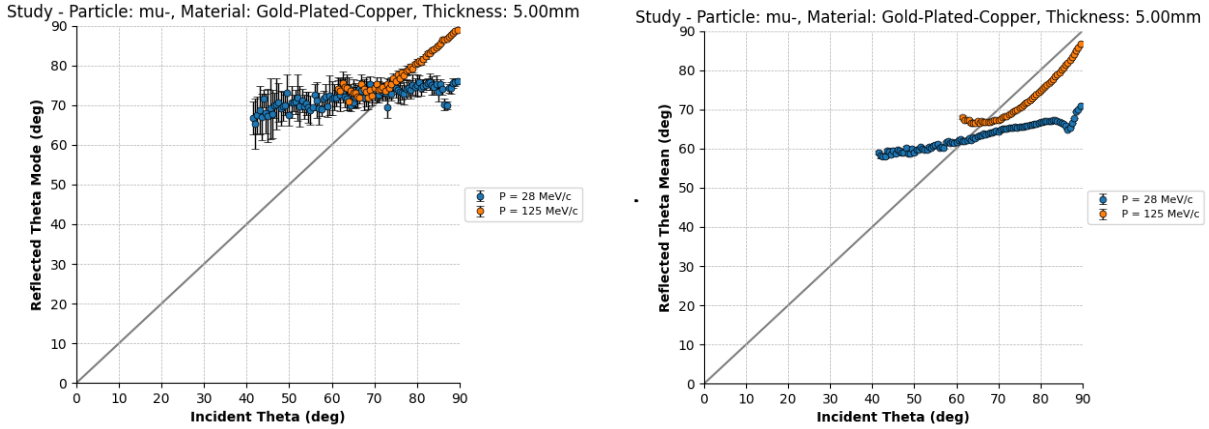

FIGURE 24: Plots of the mode (left) and mean (right) of the reflected angle distributions (in a range where there is notable reflection) of μ^- reflecting off of a gold-plated copper plate, at an incident momentum of 28 MeV/c and 125 MeV/c.

From these series of plots, there are a number of notable behaviours. First, for all materials at 125 MeV/c, the peak of the reflected momentum distribution is concentrated at large incident angles and at the incident momentum. At 28 MeV/c, the peak of the reflected momentum distributions lies below the incident momentum. The distance below appears to depend on the density of the material. For glass, the peak lies only a small amount below the incident momentum, whereas for copper and gold-plated copper, the peak lies further below the incident momentum. Next, for copper and glass, the mode of the reflected angle distributions appears to take a piecewise linear form. Notable for the 125 MeV/c incident momentum cases, the mode tends towards the identity line for large incident angles. For the 28 MeV/c incident momentum cases, the mode tends towards the identity line for a section near large incident angles, but then deviates below the identity line for the largest incident angles.

As seen in the appendix, these trends persist with the various other materials simulated in the same manner.

3.1.9 Gold-Plating Thickness Study

One of the final studies performed for this flat scattering experiment (to date) was a comparison between the reflection, transmission, absorption, and decay curves for gold plating of different thicknesses. In the gold-plated copper cases from previous studies, it was observed that there was a defect in these curves at a fixed high incident angle. It appeared that the behaviour looked similar to that of a strictly copper plate for incident angles below the defect and that of a strictly gold plate for incident angles above the defect (with a slight negative offset). To verify that this defect was indeed a result of the plating and to check whether it varied with the thickness of the plating, a complete batch of simulations and the corresponding plots were produced to compare the plating thicknesses of 5 µm, 10 µm and 15 µm.

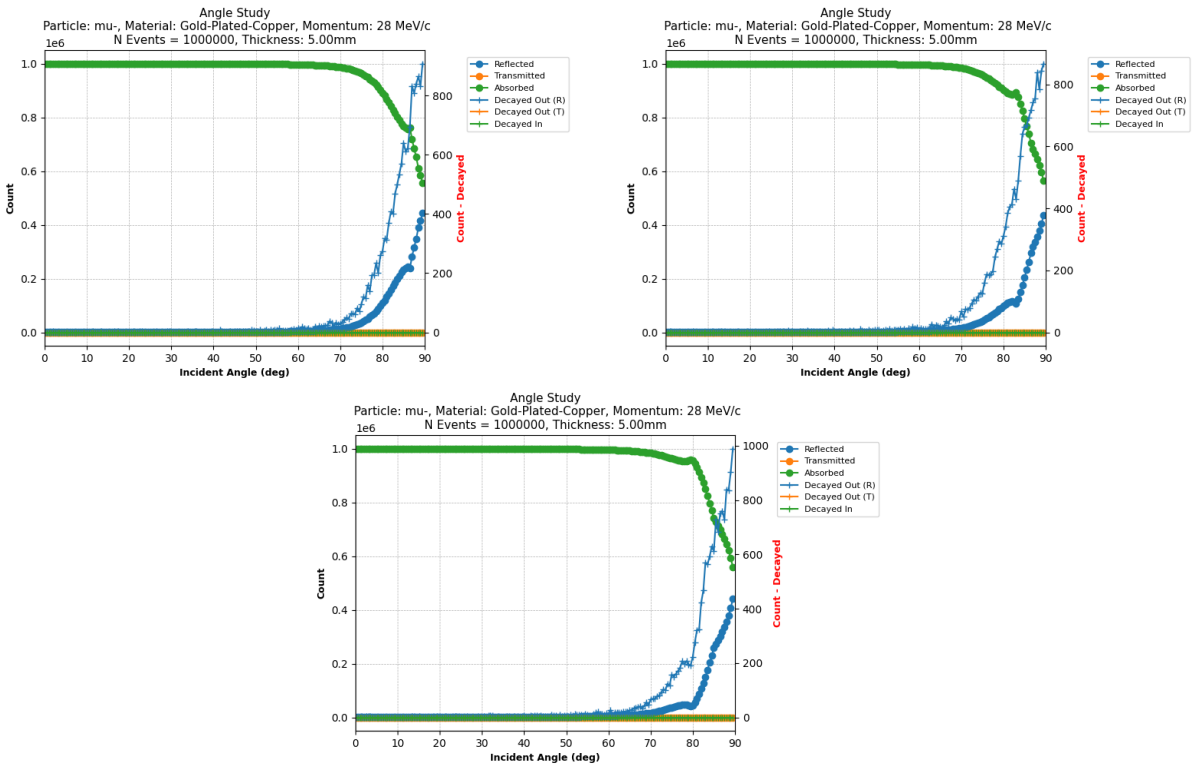

FIGURE 25: Plots of the counts of reflected, transmitted, absorbed, and decayed μ^- with a gold-plated copper scattering plate (5 µm, top left, 10 µm, top right, 15 µm, bottom, plating thickness, respectively) over the whole range of incident angles $(0^\circ, 90^\circ)$, at an incident momentum of 28 MeV/c.

From the plots in Fig. 25, it is clear that as the plating thickness doubles and triples, the defect, which starts at an incident angle of roughly 86°, shifts roughly a proportional amount to the left. Intuitively, as the gold-plating thickness is increased, the incident angle will be smaller for the muon to pierce the copper layer. For large incident angles, the effective cross section of the gold plating may be large enough so that the interaction of the muons with the plate occurs solely in the plating, which would explain the behaviour exhibited at the largest incident angles.

This behaviour of the defect is also visible in plots of the outgoing momentum distributions and of the modes and means of the reflected angle distributions.

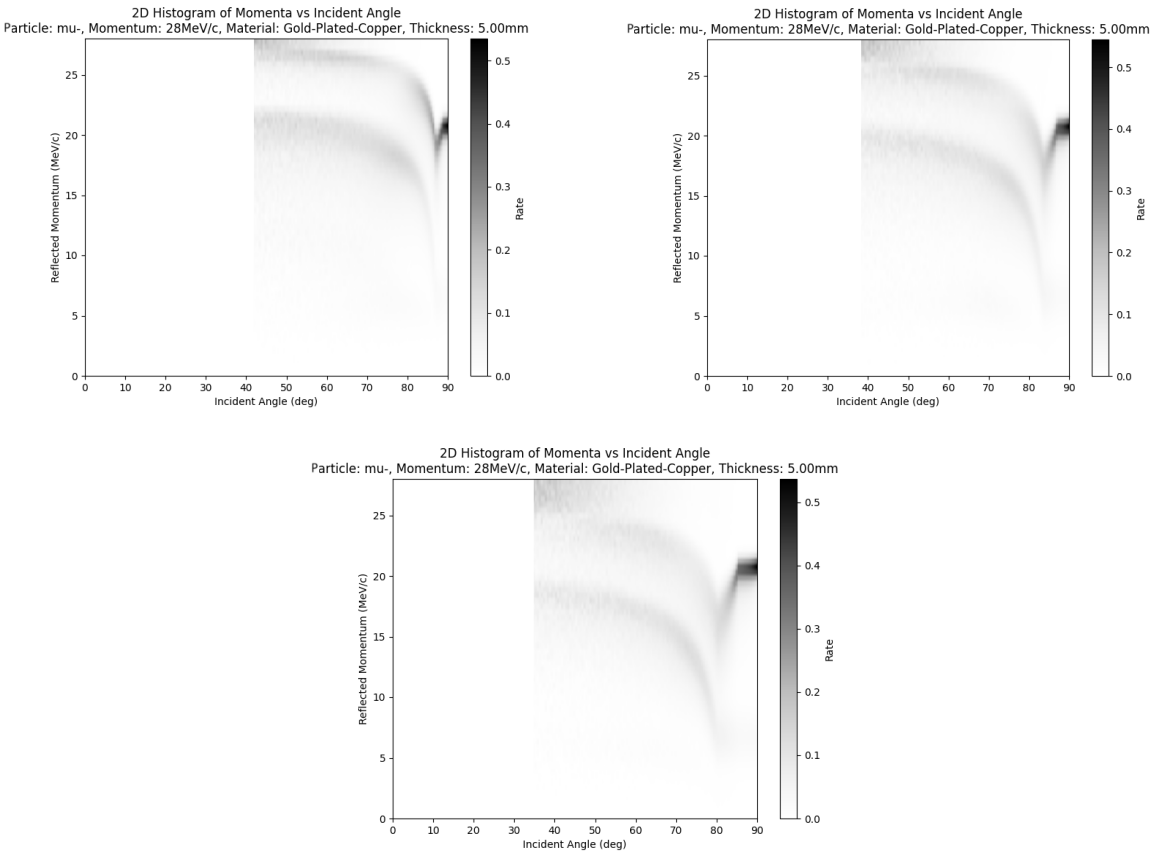

FIGURE 26: 2D histograms of the reflected momentum distributions (in a range where there is notable reflection) of μ^- reflecting off of a gold-plated copper plate (5 µm, top left, 10 µm, top right, 15 µm, bottom, plating thickness, respectively) over the whole range of incident angles $(0°, 90°)$, at an incident momentum of $28\,\mathrm{MeV}/c$.

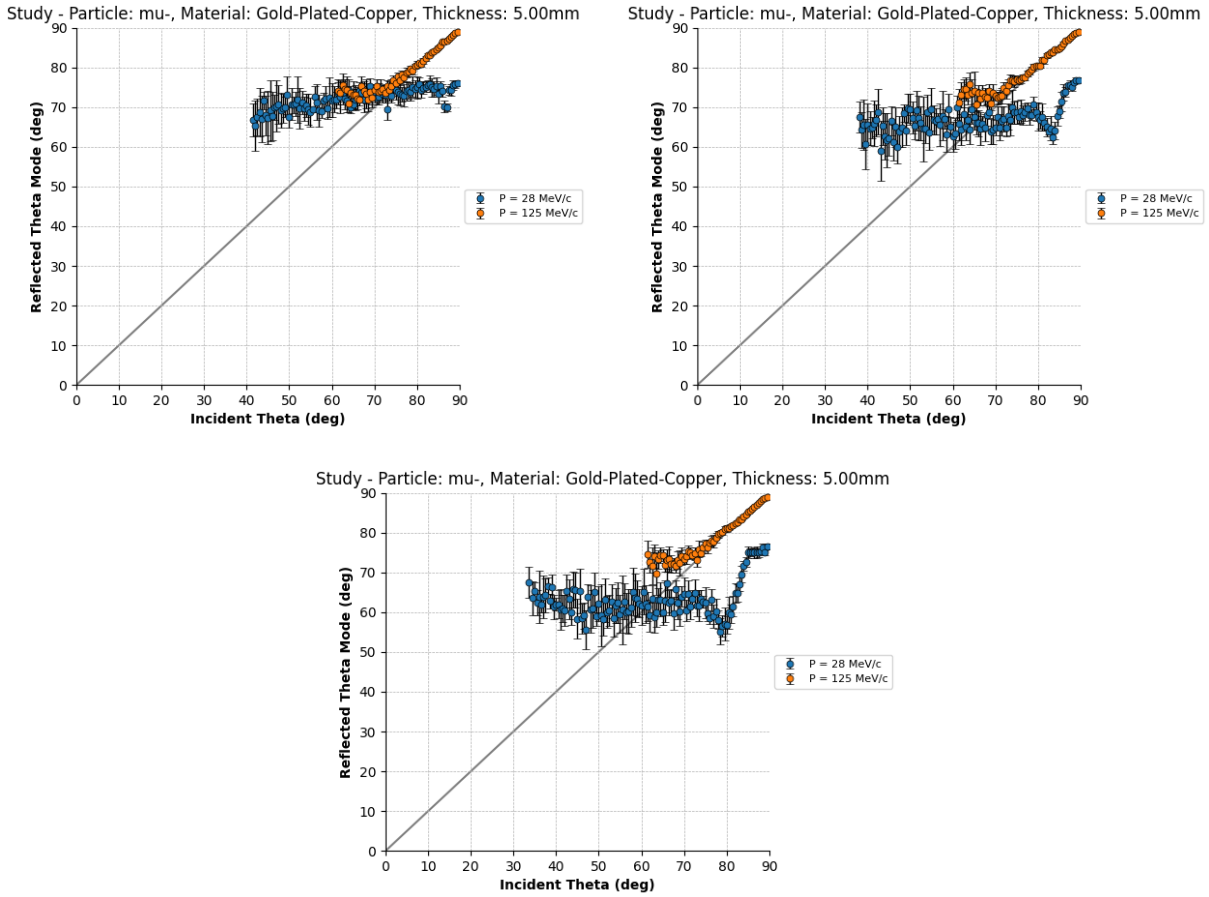

FIGURE 27: Plots of the mode of the reflected angle distributions of μ^- reflecting off of a gold-plated copper plate (5 µm, top left, 10 µm, top right, 15 µm, bottom, plating thickness, respectively) over the whole range of incident angles $(0°, 90°)$, at an incident momentum of 28 MeV/c.

In Figs. 26 and 27, we can see the same behaviour of the gold plating that was exhibited in Fig. 25 with even more clarity.

3.2 Tapered Capillaries

Analysis for tapered capillary simulations for various combinations of profiles, materials, coatings, etc., is an ongoing process. Further decisions need to be made, with the knowledge acquired from the flat scattering simulation results, to narrow the configuration space of possible tapered capillary simulations. Once this has been done, simulations can be run and a similar type of analysis can be performed with the simulation results. In particular, this analysis will look at the enhancement of beam density, as demonstrated in Refs. [3, 5], and also the potential for a beam cooling effect (as outlined in the background section of this report).

4 Conclusions

The studies performed on flat scattering using Geant4 simulation provide information on the characteristics of scattering of low-energy particles on various flat material surfaces. While there is still much work to be done to learn from these flat scattering results to guide simulation configuration decisions for the tapered capillary simulation and its analysis, these results are a step in that direction. It has become evident that a notable rate of reflection of particles occurs primarily at high incident angles. For higher incident momenta, reflected particles lose less momenta (although this decreases for lower incident angles). Less dense materials

appear to decrease this momentum loss at all incident angles. Furthermore, the distribution of modes of the reflected angle of particles tends towards the identity line for large incident angles and high incident momenta. For lower incident momenta, the mode tends towards the identity line for large incident angles up to a point where it falls below the identity line (and tends towards a flat line) for the highest incident angles. At all incident momenta, this distribution of modes appears to be a piecewise-linear function. This is an interesting and unexpected behaviour.

Moving forward, there are many more things to investigate. First, the distribution of modes could be fit to some piecewise-linear function, to develop a model of reflection. This model could then be applied to the tapered capillaries to help determine which capillary profile provides optimal density enhancement and perhaps a beam cooling effect. Furthermore, once the tapered capillary simulation is finalised, perhaps direct analysis of the output particle beam features will indicate whether or not tapered capillaries may be of use in future muon accelerator collider or fixed-target experiments.

In general, not only has this project helped to provide more insight into the characterisation of flat scattering of low-energy particles on flat surfaces, it has also provided a great opportunity to develop Geant4 simulation skills, data analysis experience, and a greater understanding of accelerator and particle physics.

5 Acknowledgements

I would like to extend my gratitude to my supervisor, Dr. Massimo Giovannozzi, for his support, guidance, and mentorship throughout this research project, and to Carlo Emilio Montanari for his invaluable assistance in learning CERN software and workflow optimisation (without which progress on this project would not have been possible). I further extend my gratitude to the whole CERN Summer Student Programme for the amazing summer experience and the opportunity to learn from and work alongside leading researchers in physics. I also acknowledge the support of the Natural Sciences and Engineering Research Council of Canada (NSERC) and the Institute of Particle Physics for its support via the IPP Summer Student Fellowship Programme.

References

[1] D. Ciarniello. CERN Summer Student Project Github Repository. https://github.com/deanciarniello/CERN-Summer-Student-Project, 2023.

[2] K. S. Khaw, A. Adelmann, M. Backhaus, N. Berger, M. Daum, M. Giovannozzi, K. Kirch, A. Knecht, A. Papa, C. Petitjean, F. Renga, M. Sakurai, and P. Schmidt-Wellenburg. Search for the muon electric dipole moment using frozen-spin technique at PSI, 2022.

[3] Takao Kojima, Dai Tomono, Tokihiro Ikeda, Katsuhiko Ishida, Yoshio Iwai, Masahiko Iwasaki, Yasuyuki Matsuda, Teiichiro Matsuzaki, and Yasunori Yamazaki. Density enhancement of muon beams with tapered glass tubes. *Journal of The Physical Society of Japan*, 76, 09 2007.

[4] M. Steck. Beam cooling. https://wiki.jlab.org/ciswiki/images/c/cc/Beam_cooling-Steck.pdf, September 2011.

[5] Dai Tomono, Takao Kojima, Katsuhiko Ishida, Tokihiro Ikeda, Yoshio Iwai, Makoto Tokuda, Yuu Kanazawa, Yasuyuki Matsuda, Teiichiro Matsuzaki, Masahiko Iwasaki, and Yasunori Yamazaki. Focusing effect of mev muon beam with a tapered capillary method. *Journal of The Physical Society of Japan*, 80, 04 2011.

A Appendix

Additional 28 MeV/c and 125 MeV/c μ^- Materials

Gold

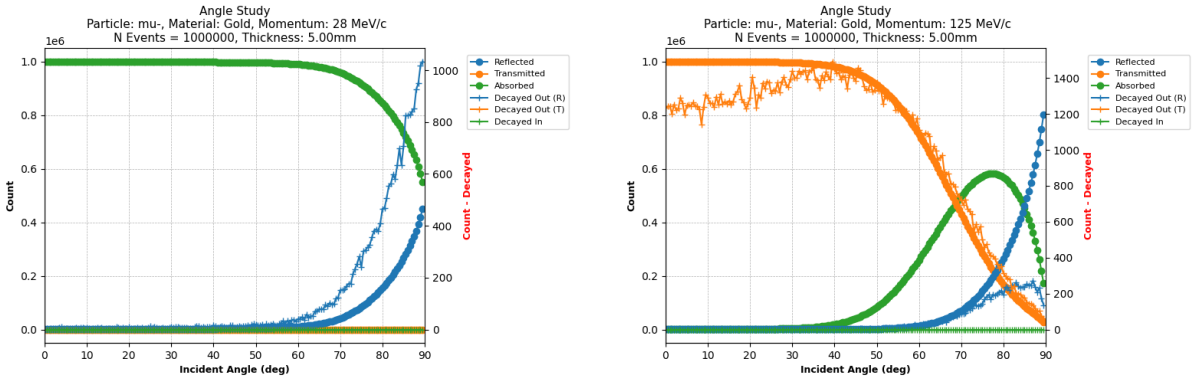

FIGURE 28: Plots of the counts of reflected, transmitted, absorbed, and decayed μ^- with a gold scattering plate over the whole range of incident angles $(0°, 90°)$, at incident momenta of 28 MeV/c (left) and 125 MeV/c (right).

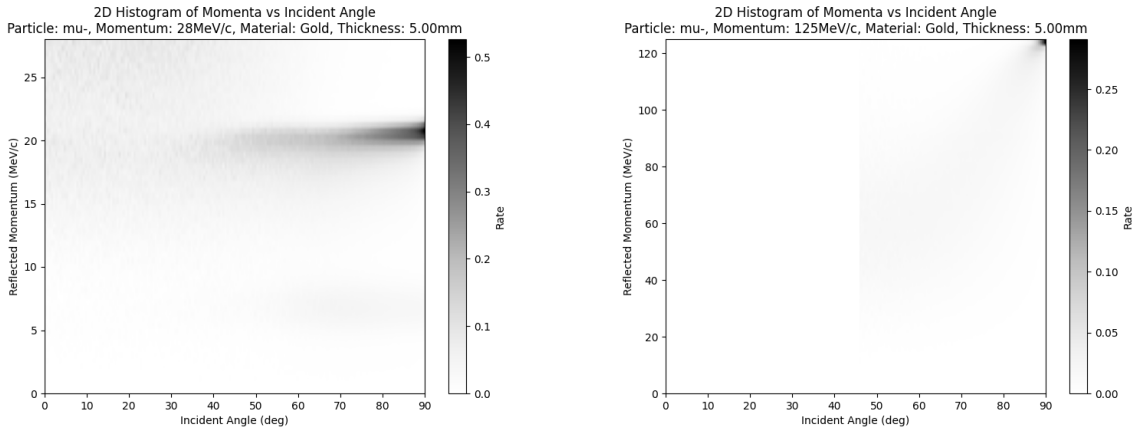

FIGURE 29: 2D histograms of the reflected momentum distributions (in a range where there is notable reflection) of μ^- reflecting off of a gold plate, at incident momenta of 28 MeV/c (left) and 125 MeV/c (right).

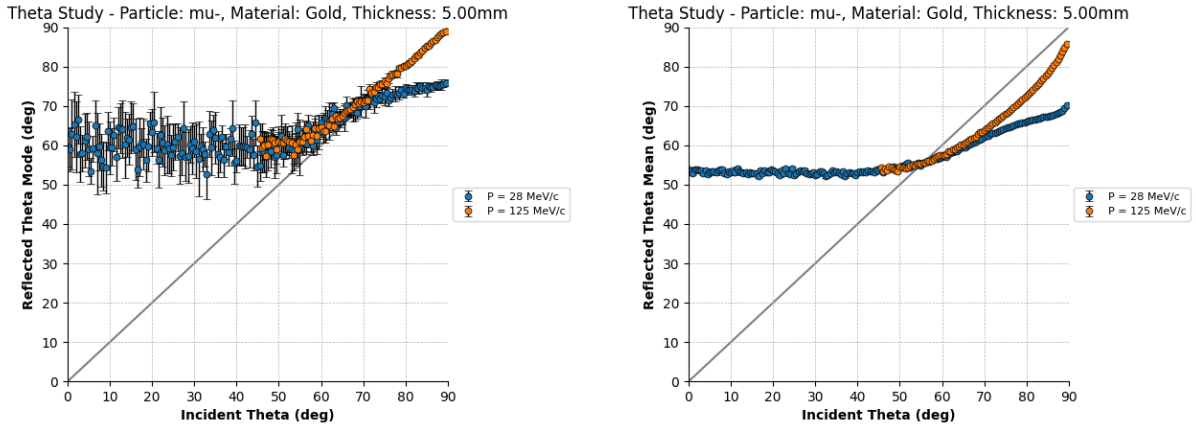

FIGURE 30: Plots of the mode (left) and mean (right) of the reflected angle distributions (in a range where there is notable reflection) of μ^- reflecting off of a gold plate, at an incident momentum of $28\,\mathrm{MeV}/c$ and $125\,\mathrm{MeV}/c$.

Iron

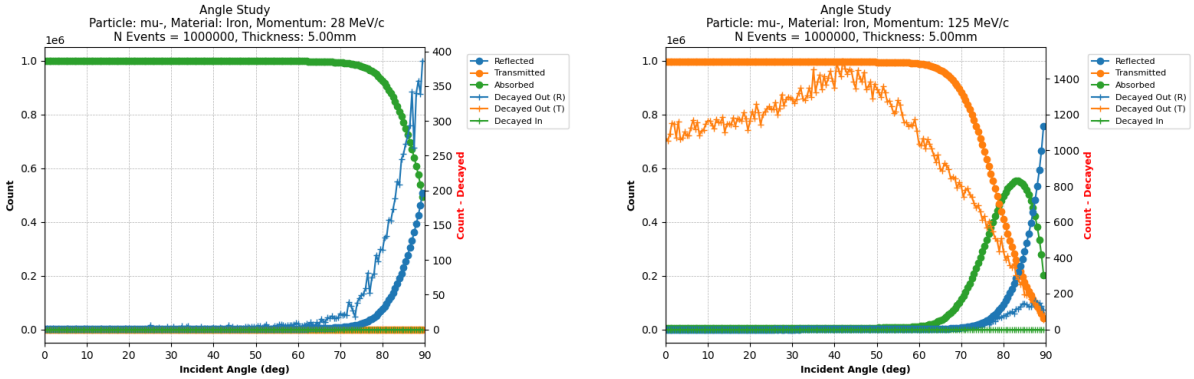

FIGURE 31: Plots of the counts of reflected, transmitted, absorbed, and decayed μ^- with a iron scattering plate over the whole range of incident angles $(0°, 90°)$, at incident momenta of $28\,\mathrm{MeV}/c$ (left) and $125\,\mathrm{MeV}/c$ (right).

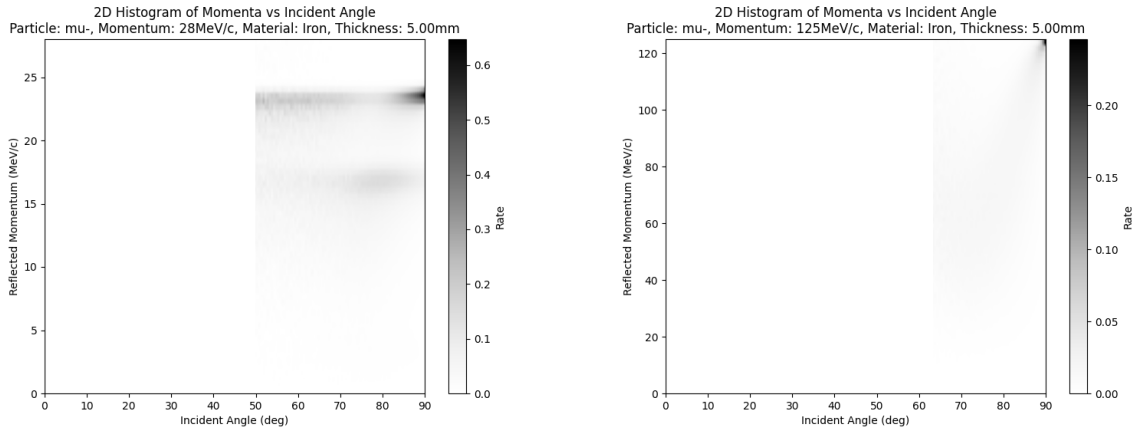

FIGURE 32: 2D histograms of the reflected momentum distributions (in a range where there is notable reflection) of μ^- reflecting off of a iron plate, at incident momenta of $28\,\mathrm{MeV}/c$ (left) and $125\,\mathrm{MeV}/c$ (right).

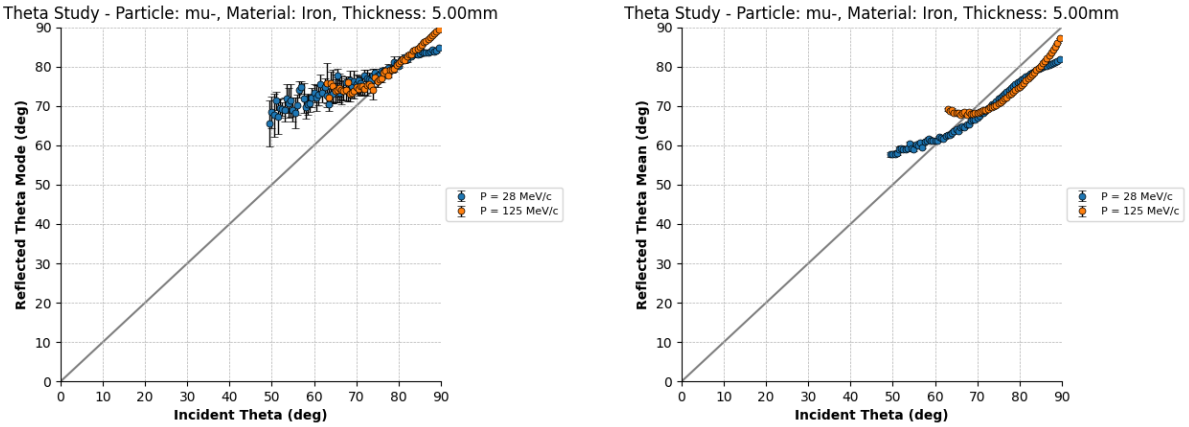

FIGURE 33: Plots of the mode (left) and mean (right) of the reflected angle distributions (in a range where there is notable reflection) of μ^- reflecting off of a iron plate, at an incident momentum of 28 MeV/c and 125 MeV/c.

Silver

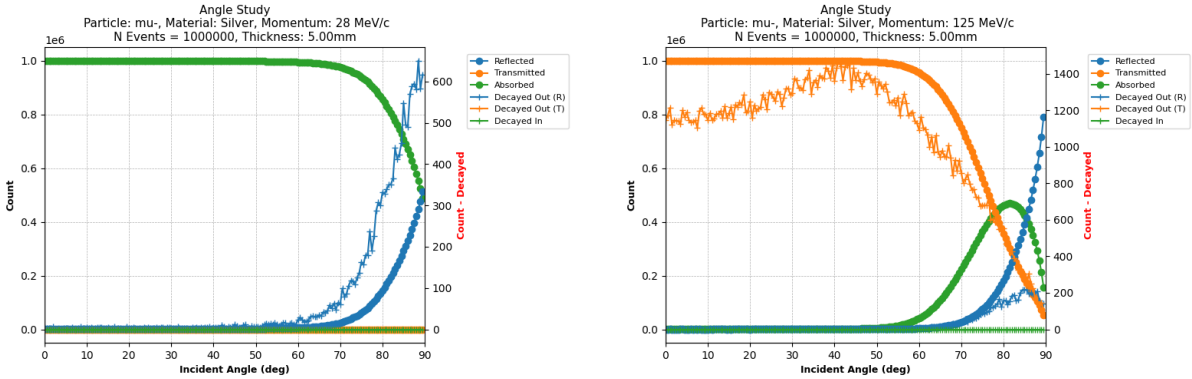

FIGURE 34: Plots of the counts of reflected, transmitted, absorbed, and decayed μ^- with a silver scattering plate over the whole range of incident angles $(0°, 90°)$, at incident momenta of 28 MeV/c (left) and 125 MeV/c (right).

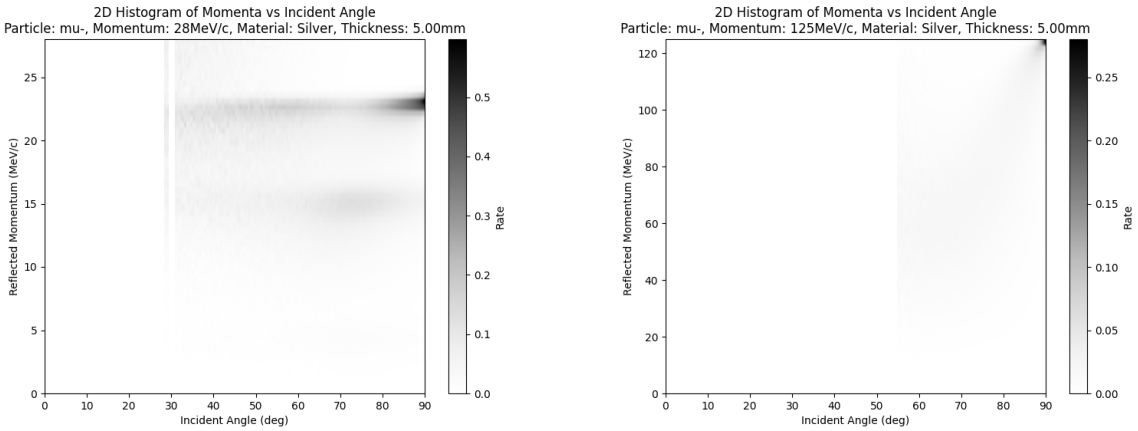

FIGURE 35: 2D histograms of the reflected momentum distributions (in a range where there is notable reflection) of μ^- reflecting off of a silver plate, at incident momenta of 28 MeV/c (left) and 125 MeV/c (right).

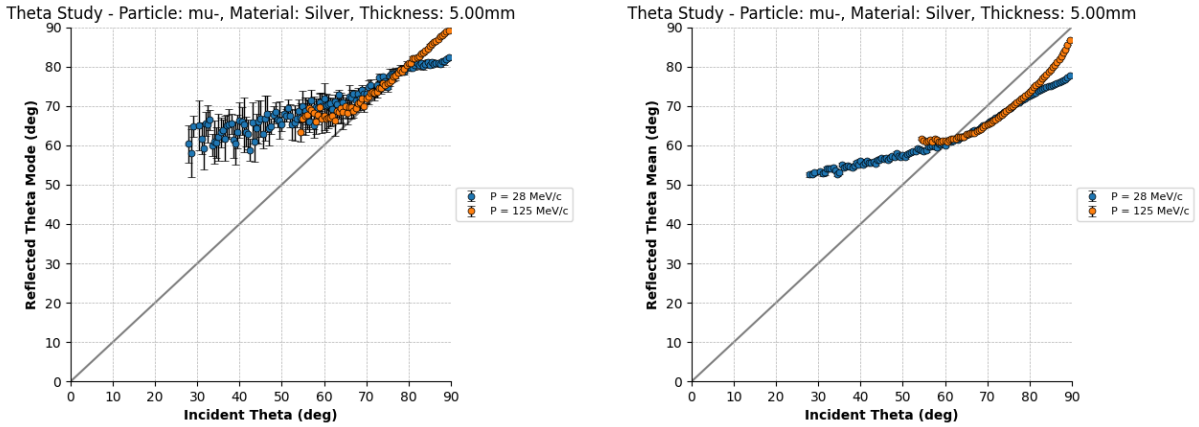

FIGURE 36: Plots of the mode (left) and mean (right) of the reflected angle distributions (in a range where there is notable reflection) of μ^- reflecting off of a silver plate, at an incident momentum of 28 MeV/c and 125 MeV/c.

Stainless Steel

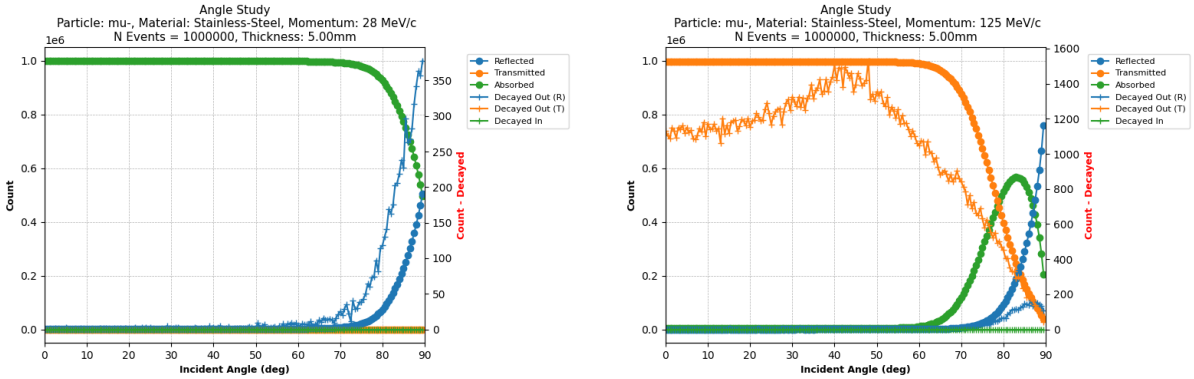

FIGURE 37: Plots of the counts of reflected, transmitted, absorbed, and decayed μ^- with a stainless steel scattering plate over the whole range of incident angles $(0°, 90°)$, at incident momenta of 28 MeV/c (left) and 125 MeV/c (right).

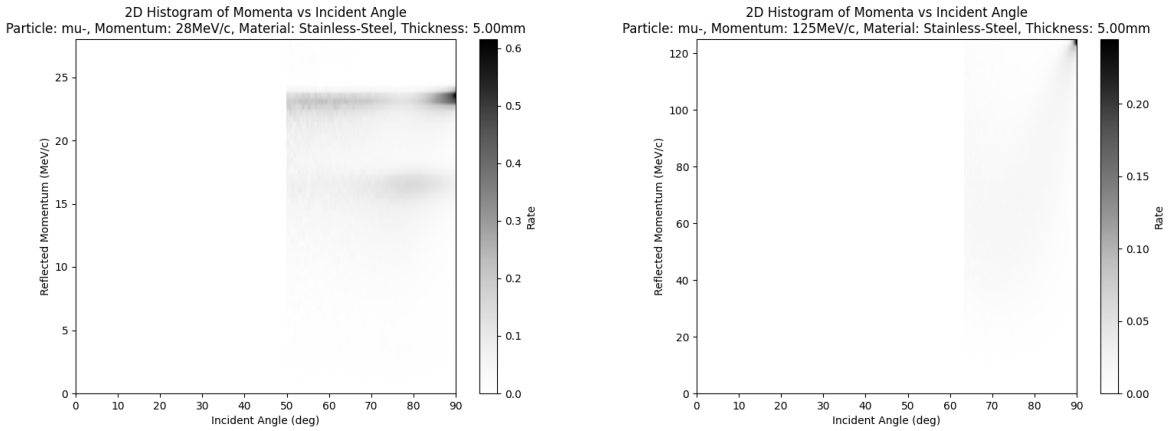

FIGURE 38: 2D histograms of the reflected momentum distributions (in a range where there is notable reflection) of μ^- reflecting off of a stainless steel plate, at incident momenta of 28 MeV/c (left) and 125 MeV/c (right).

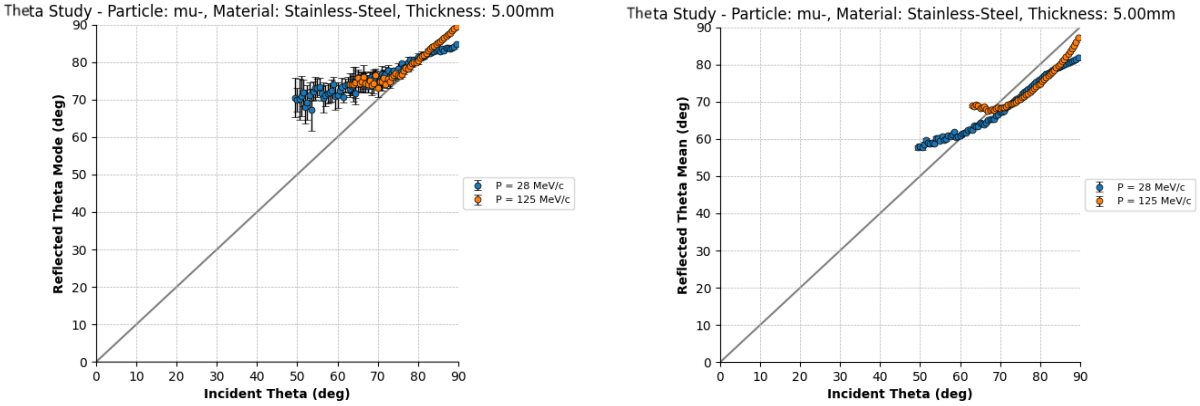

FIGURE 39: Plots of the mode (left) and mean (right) of the reflected angle distributions (in a range where there is notable reflection) of μ^- reflecting off of a stainless steel plate, at an incident momentum of 28 MeV/c and 125 MeV/c.

Aluminium

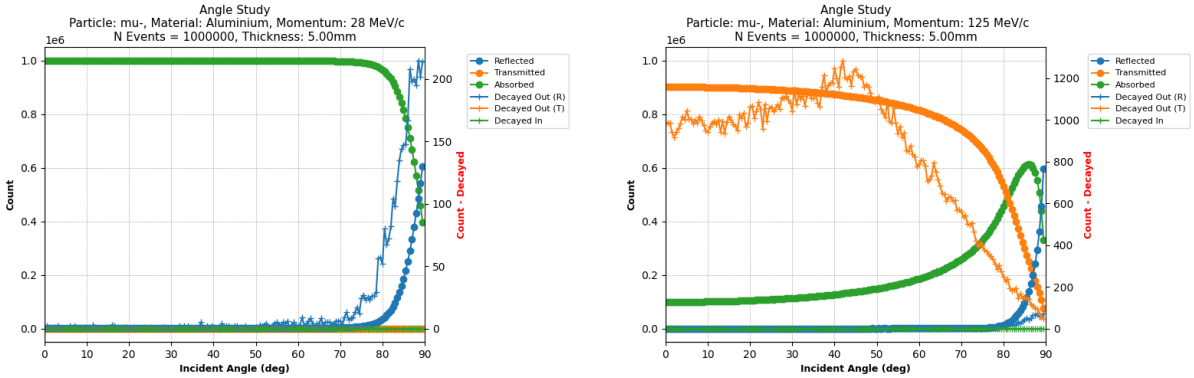

FIGURE 40: Plots of the counts of reflected, transmitted, absorbed, and decayed μ^- with a aluminium scattering plate over the whole range of incident angles $(0^\circ, 90^\circ)$, at incident momenta of 28 MeV/c (left) and 125 MeV/c (right).

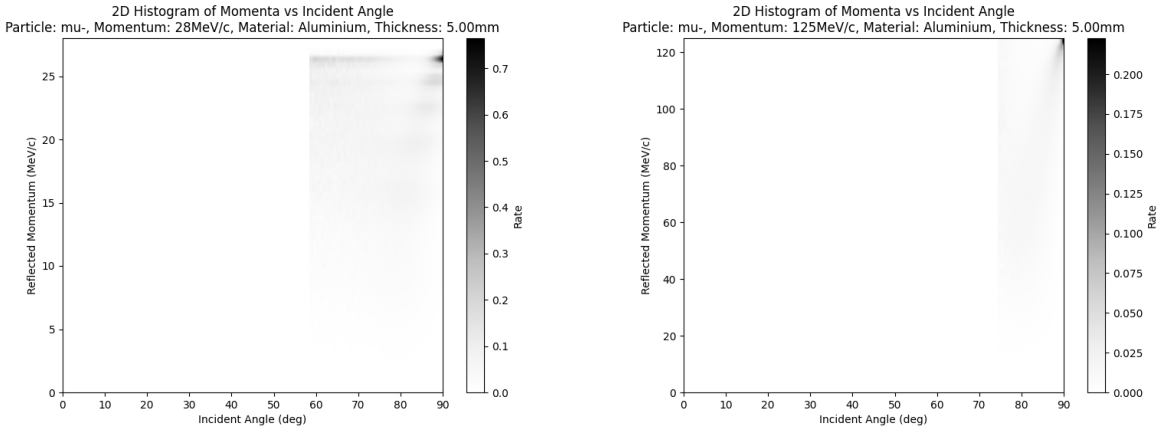

FIGURE 41: 2D histograms of the reflected momentum distributions (in a range where there is notable reflection) of μ^- reflecting off of a aluminium plate, at incident momenta of 28 MeV/c (left) and 125 MeV/c (right).

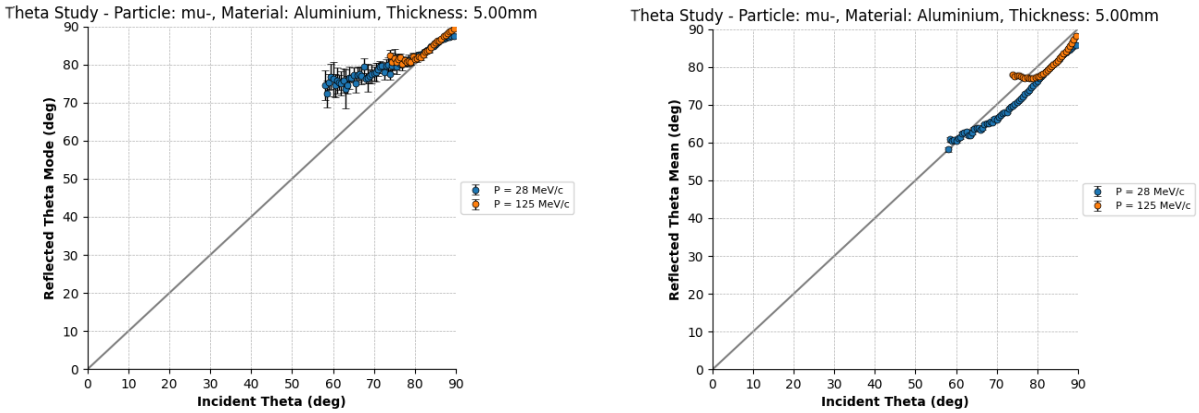

FIGURE 42: Plots of the mode (left) and mean (right) of the reflected angle distributions (in a range where there is notable reflection) of μ^- reflecting off of a aluminium plate, at an incident momentum of $28\,\mathrm{MeV}/c$ and $125\,\mathrm{MeV}/c$.

Brass

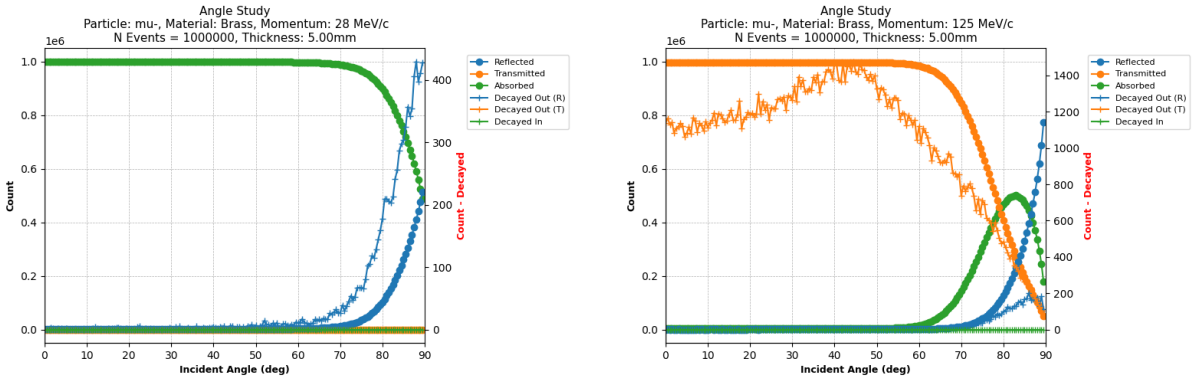

FIGURE 43: Plots of the counts of reflected, transmitted, absorbed, and decayed μ^- with a brass scattering plate over the whole range of incident angles $(0°, 90°)$, at incident momenta of $28\,\mathrm{MeV}/c$ (left) and $125\,\mathrm{MeV}/c$ (right).

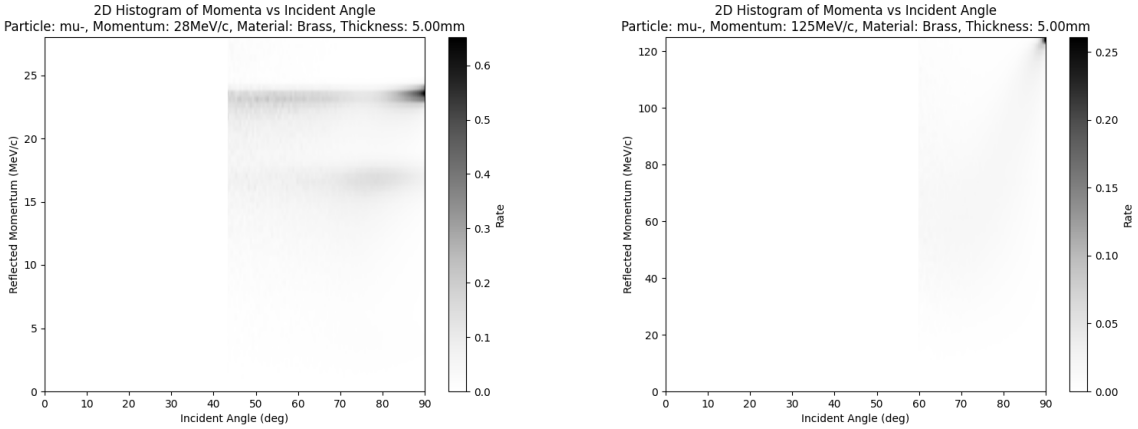

FIGURE 44: 2D histograms of the reflected momentum distributions (in a range where there is notable reflection) of μ^- reflecting off of a brass plate, at incident momenta of $28\,\mathrm{MeV}/c$ (left) and $125\,\mathrm{MeV}/c$ (right).

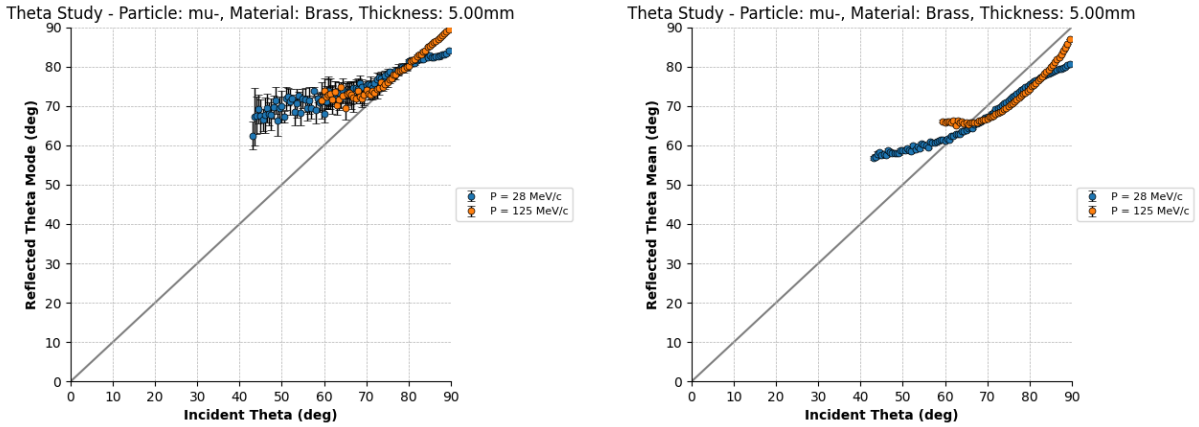

FIGURE 45: Plots of the mode (left) and mean (right) of the reflected angle distributions (in a range where there is notable reflection) of μ^- reflecting off of a brass plate, at an incident momentum of $28\,\mathrm{MeV}/c$ and $125\,\mathrm{MeV}/c$.

Bronze

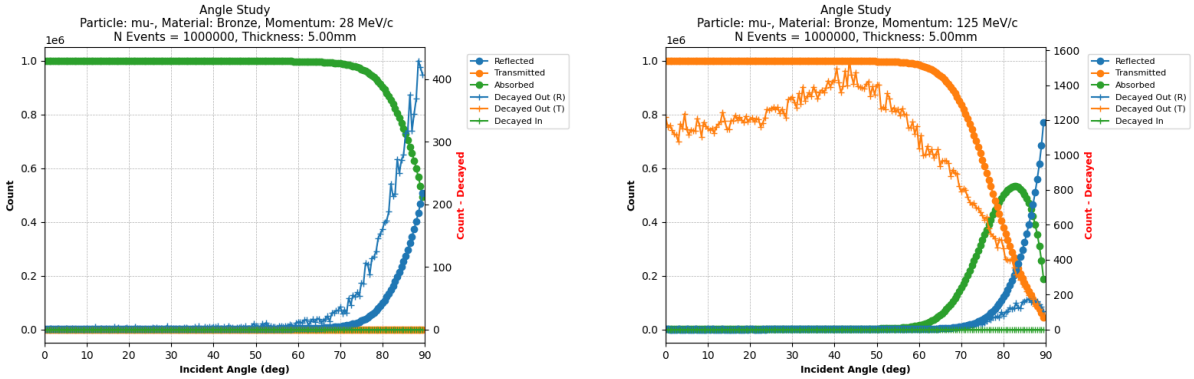

FIGURE 46: Plots of the counts of reflected, transmitted, absorbed, and decayed μ^- with a bronze scattering plate over the whole range of incident angles $(0°, 90°)$, at incident momenta of $28\,\mathrm{MeV}/c$ (left) and $125\,\mathrm{MeV}/c$ (right).

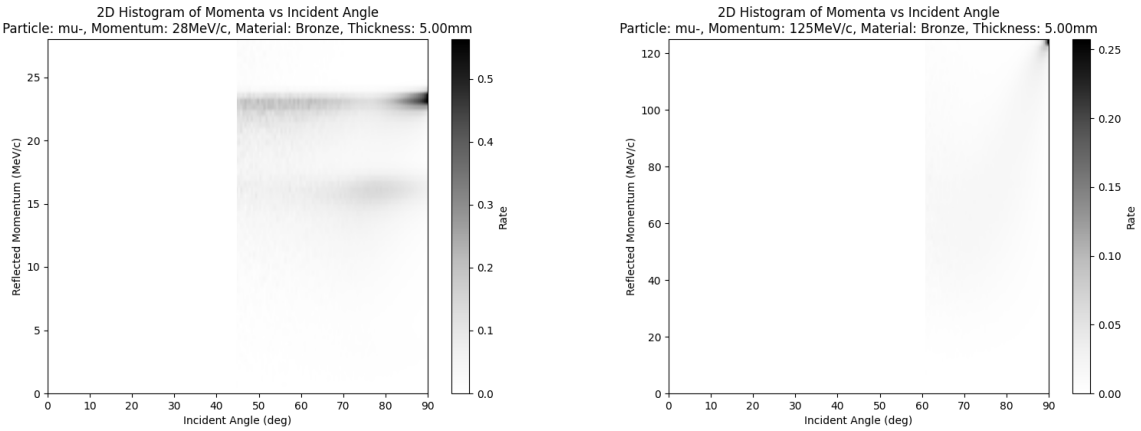

FIGURE 47: 2D histograms of the reflected momentum distributions (in a range where there is notable reflection) of μ^- reflecting off of a bronze plate, at incident momenta of $28\,\mathrm{MeV}/c$ (left) and $125\,\mathrm{MeV}/c$ (right).

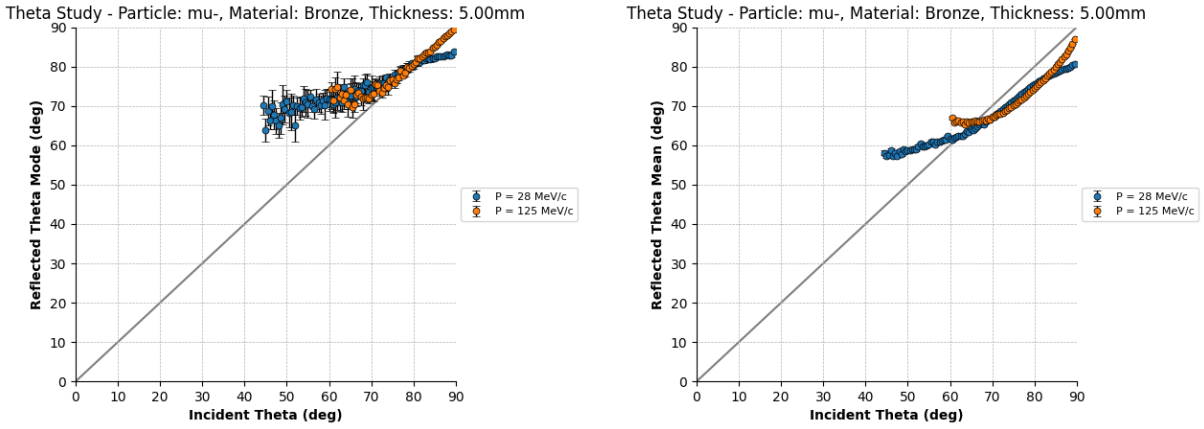

FIGURE 48: Plots of the mode (left) and mean (right) of the reflected angle distributions (in a range where there is notable reflection) of μ^- reflecting off of a bronze plate, at an incident momentum of $28\,\mathrm{MeV}/c$ and $125\,\mathrm{MeV}/c$.